LAWRENCE
LIVERMORE
NATIONAL
LABORATORY

UCRL-JRNL-206954

Two Dimensional Simulations of Plastic-Shell, Direct-Drive Implosions on OMEGA

P. B. Radha, V. N. Goncharov, T. J. B. Collins, J. A. Delettrez, Y. Elbaz, V. Yu. Glebov, R. L. Keck, D. E. Keller, J. P. Knauer, J. A. Marozas, F. J. Marshall, P. W. McKenty, D. D. Meyerhofer, S. P. Regan, T. C. Sangster, D. Shvarts, S. Skupsky, Y. Srebro, R. P. J. Town, C. Stoeckl

October 1, 2004

Physics of Plasmas

Two-Dimensional Simulations of Plastic-Shell, Direct-Drive Implosions on OMEGA

P. B. Radha, V. N. Goncharov, T. J. B. Collins, J. A. Delettrez, Y. Elbaz,†
V. Yu. Glebov, R. L. Keck, D. E. Keller, J. P. Knauer, J. A. Marozas, F. J. Marshall,
P. W. McKenty, D. D. Meyerhofer,* S. P. Regan, T. C. Sangster, D. Shvarts,†
S. Skupsky, Y. Srebro,† R. P. J. Town,‡ and C. Stoeckl

Laboratory for Laser Energetics, University of Rochester
250 E. River Road
Rochester, NY 14623

*Also Dept. of Mechanical Engineering and Physics and Astronomy

†Department of Physics, Negev Research Center
Negev, Israel

‡Lawrence Livermore National Laboratory
Livermore, CA

Abstract

Multidimensional hydrodynamic properties of high-adiabat direct-drive plastic-shell implosions on the OMEGA laser system [T. R. Boehly *et al*., Opt. Commun. **133**, 495 (1997)] are investigated using the multidimensional hydrodynamic code, *DRACO*. Multimode simulations including the effects of nonuniform illumination and target roughness indicate that shell stability during the acceleration phase plays a critical role in determining target performance. For thick shells that remain integral during the acceleration phase, target yields are significantly reduced by the combination of the long-wavelength ($\ell < 10$) modes due to surface roughness and beam imbalance and the intermediate modes ($20 \leq \ell \leq 50$) due to single-beam nonuniformities. The neutron-production rate for these thick shells truncates relative to one-dimensional (1-D) predictions. The yield degradation in the thin shells is mainly due to shell breakup at short wavelengths ($\lambda \sim \Delta$, where Δ is the in-flight shell thickness). The neutron-rate curves for the thinner shells have significantly lower amplitudes and a fall-off that is less steep than 1-D rates. *DRACO* simulation results are consistent with experimental observations.

I. Introduction

In direct-drive inertial confinement fusion (ICF),[1] nominally identical beams of a laser are incident on a nearly spherically symmetric target. The target's outer surface ablates, driving the shell inward like a rocket. The shell first accelerates and then, after the laser drive is turned off, coasts before decelerating toward peak compression; disassembly then follows. The goal is to implode the target, resulting in sufficiently high temperatures and densities to propagate a self-sustaining burn wave through the target, giving rise to energetic neutrons with a total energy output greater than the laser energy. Ignition target designs require layers of cryogenic deuterium–tritium (DT) ice[2] and relatively high laser energies such as those that will be available on the National Ignition Facility (NIF).[3] To provide an understanding of target dynamics, a large number of implosions on the 60-beam OMEGA laser[4] have been devoted to warm capsules,[5–8] which include plastic (CH) shells filled with deuterium (D_2) gas. While a number of papers have been written on the experimental results from CH-shell implosions on OMEGA,[5–8] the wavelength range of nonuniformities that influence the fusion yield has been an outstanding question.

In this paper, a detailed analysis of high-adiabat CH-shell implosions using one- and two-dimensional simulations and analytical modeling is performed. This work identifies, by using the hydrodynamic code *DRACO*,[9] the nonuniformity seeds that influence target performance. Mechanisms that influence yields are also identified. In addition, comparisons to experimental results are presented.

Imperfect illumination and target roughness seed the nonuniformity growth in direct-drive implosions. The incident laser irradiation on the target includes nonuniformities that result from energy and power imbalances among the beams and from nonuniformities within each beam. The former results in long-wavelength ($\ell < 10$, where $\ell = 2\pi R/\lambda$ is the Legendre mode number, R is the target radius, and λ is the nonuniformity wavelength) perturbations that lead to an overall deformation of the shell.

The latter are manifest in the intermediate-wavelength ($10 < \ell < 50$) and short-wavelength ($\ell > 50$) nonuniformities that can lead to shell breakup during the acceleration phase as well as a disruption in final fuel assembly.

Nonuniformities grow due to the Rayleigh–Taylor (RT) instability[10] during the acceleration phase of the implosion. The RT growth rates are smaller than classical values due to the ablative effects.[10–13] Nevertheless, the RT growth factors of the short-wavelength modes in the thin shells are large enough to compromise shell integrity during the acceleration phase. Shell breakup results in degradation of the shell compressibility, which leads to a reduction in the final core temperature and density and, consequently, a reduction in the neutron-production rates.

Nonuniformity growth during the coasting and deceleration phases of the implosions is seeded by feedthrough to the inner surface of the shell. Fuel–pusher interface distortions grow significantly during the coasting phase because of convergent effects (Bell–Plesset growth).[15,16] Further, truncation of the neutron-production rate occurs due to the flow of fuel into the colder bubbles at the D_2–CH interface during shell deceleration. Truncation is also caused by the increased heat conduction out of the core due to the larger surface area caused by shell distortions.

This paper is organized as follows: One-dimensional and multidimensional hydrodynamic modeling are described in Sec. II. Overall shell dynamics is discussed in Sec. III. In Sec. IV the four phases of the implosion (shock transit, acceleration, coasting, and deceleration) are analyzed in the context of single-mode growth. In Sec. V multidimensional simulations of beam-to-beam imbalances and single-beam nonuniformity are described, and the combined effects of all nonuniformity sources are discussed. Conclusions are presented in Section VI.

II. Radiation-Hydrodynamics Modeling

The one-dimensional (1-D) target dynamics discussed in this paper is modeled using the code *LILAC*,[17] which has been described extensively in the literature and is not discussed any further.

Multidimensional behavior (2-D) of plastic targets is modeled using the code *DRACO*.[9] *DRACO* is a one-, two-, and three-dimensional arbitrary Lagrangian Eulerian[18] (ALE) code based on a structured mesh. The implosions described in this paper are simulated in one and two dimensions. Shocks are treated using Wilkins' scheme.[19] Several artificial grid-smoothing algorithms are available to control numerical grid distortions (bowties and herringbone distortions). These are based on Refs. 18–20; only Ref. 20 is used in this work.

In a purely Lagrangian mode, interfaces between materials are maintained at cell edges; however, a significant growth of perturbations results in a severely distorted grid. As a result, the grid must be "rezoned" for the simulation to proceed. The new grid can be constructed using several prescriptions. While some grid movement options are heuristically derived, others are based on Winslow-regridding–type[21] schemes. *DRACO* allows for cells with mixed materials resulting from this grid rezoning. Rezoning is possible through a first-order (donor-cell) or a direction-split second-order scheme.[22] Material interfaces are reconstructed before every rezoning step using a scheme based on Young's,[24] which has been extended to allow for distorted Lagrangian cells. In this scheme, the interface between materials in a cell is represented by a straight line; the slope of this line is obtained through the gradient of the fractional volumes occupied by the material in the neighboring cells.

The pressure in each mixed-material cell is obtained by adding the partial pressures of the constituent cell materials. A single temperature for the materials in the cell is obtained using the prescription described in Ref. 23. While this interface tracking

scheme cannot be used to model turbulent regimes,[24] it has been used to model the highly nonlinear growth of buried layers that burn through to the corona.[9]

Processes, such as heat conduction, radiation transport, etc., are treated using an operator splitting procedure. *DRACO* includes the deposition of laser energy through ray tracing and inverse bremsstrahlung. Both normal-incidence laser energy deposition and the ray-trace approach are used in this work. Since normal incidence does not include refractive energy losses, it can significantly overestimate the energy coupled to the target. For normal incidence simulations, the laser pulse shape is iteratively adjusted in 1-D simulations to provide the same overall dynamics of the implosion, including shock-breakout times, the final convergence of the shell, ablation velocities, density scale lengths, etc., as obtained with a full ray trace. This modified pulse shape is used in two-dimensional (2-D) simulations involving modes ≥20. Spherically symmetric 2-D simulations with this modified pulse shape compare very well with 1-D simulations using a full ray trace. For simulations that include only long-wavelength modes ($\ell \leq 10$), we use a refractive ray trace. This ray trace uses a quasi-1-D scheme, where rays are not allowed to cross angular sector boundaries. This scheme accounts for refractive losses reasonably accurately only when the distortions are of relatively long wavelengths. In this technique, an angular spectrum describing the distribution of energy with angle of incidence is launched from a chosen surface each time step. This distribution takes into account both the single-beam ray distribution and beam overlap. In the limit of a spherically symmetric problem, this approach yields the same results as a full ray trace.

Several equation-of-state options (ideal gas, *SESAME*,[25] Thomas–Fermi[26] and QEOS) are available; the analytic Thomas–Fermi formulation is used for the simulations described in this work. Heat conduction and multigroup diffusive radiation transport are included. Tabular opacities assuming local thermal equilibrium are used for materials in unmixed cells. An ion-number weighted opacity is used in mixed cells for radiation transport. Radiation transport is solved in parallel across several processors.

The simulations use the "group-parallel" approach where each energy group is solved on one processor and the resulting radiation energy density is broadcast to all other processors. Four radiation groups, reduced from very fine opacity tables,[28] are included in all the calculations in this work. The choice of the four energy groups is chosen to closely match the 1-D dynamics corresponding to 48 energy groups. The parallel scientific library, PetSc,[29] is used to solve the diffusion equation via a preconditioned conjugate-gradient scheme. Message Passing Interface (MPI)[30] is used to communicate among processors.

Particle production from nuclear reactions is calculated using the scheme described in Ref. 31. Alpha-particle transport and depletion of fuel material for modeling ignition are included in *DRACO* but are not necessary for simulating OMEGA target implosions.

DRACO has been tested extensively against analytic problems (shock-tube problems, blast-wave problems, etc.), against other codes (*LILAC*,[17] *ORCHID*[32]), and against the ICF postprocessor described in Ref. 33 for single-mode growth. Good agreement is obtained with the known solutions for all the problems considered.[9]

III. Shell Dynamics

This work focuses on direct-drive implosions with plastic (CH) shells filled with D_2 gas. Two cases are considered (Fig. 1): (a) a 20-μm-thick CH shell with 15 atm of D_2 with a 1-D predicted convergence ratio, CR ~13 (CR is defined as the ratio of the initial radius to the compressed radius of the fuel–shell interface at the peak of the neutron production); (b) a 27-μm-thick CH shell with 15 atm of D_2 (CR ~ 12). A 1-ns square pulse with ~23 kJ of energy is used to irradiate these targets with full beam smoothing [two-dimensional smoothing by spectral dispersion[34] (2-D SSD) with polarization smoothing (PS)].[35] Phase plates used on the beams[36–38] in these implosions have a super-Gaussian order ≃ 2.26 with a spot size (defined as the diameter that is 5% of peak

intensity) = 1000 μm. Case (a) has been chosen to illustrate implosion dynamics (Fig. 2). The laser pulse and shell acceleration history are shown in Fig. 2(a). The magnitude of the gradient of the natural logarithm of the pressure, $\left|\partial \ln P/\partial r\right|$, is shown in Fig. 2(b). The dark lines correspond to shock trajectories. The dashed line is the trajectory of the fuel–shell interface. Since the rise time of the laser is relatively fast (~200 ps), a strong shock is driven into the target, setting the shell material on a high adiabat, $\alpha \sim 5$, defined as the ratio of the pressure at a given density to the cold Fermi pressure at that density. The rarefaction wave launched at the breakout of the shock (at ~0.4 ns) from the shell reaches the ablation surface, launching a compression wave into the target. At this time the shell starts to accelerate inward as indicated by the negative acceleration in Fig. 2(a). The compression wave travels down the decreasing density gradient and breaks out of the shell as a shock (at ~0.8 ns). The shocks meet in the gas (at ~1 ns) before reaching the center. The four main phases of the implosion are shown in Fig. 2(a). The acceleration phase occurs after shock transit and continues until shortly after the laser pulse turns off (at ~1.4 ns), at which time the shell starts traveling with a constant velocity (coasting phase). Deceleration of the shell begins when the shock reflects from the center and returns to the shell (at ~1.75 ns). This impulsive deceleration is followed by a period of continuous deceleration due to pressure buildup in the gas [Fig. 2(a)].

Shock breakout is later in the thicker 27-μm implosion (at ~0.5 ns compared to ~0.4 ns). The more-massive 27-μm-thick shell moves more slowly during the coasting phase than the 20-μm-thick CH shell. It therefore coasts for a longer time (~650 ps compared to ~350 ps). The shell convergence ratio for the coasting phase, defined as the ratio of the shell radius at the beginning and end of the coasting phase, is 3.0 for the thicker shell compared to 2.2 for the thinner shell.

IV. Single-Mode Simulations

In this section, we describe the evolution of nonuniformities through single-mode simulations. The seeding of nonuniformities is described in "Shock Transit." The growth during the three phases—acceleration, coasting, and deceleration—is described in subsequent subsections.

A. Shock transit

As mentioned in Sec. III, a strong shock is launched into the shell at the beginning of the pulse. Since there is no significant acceleration of the ablation front during the shock propagation through the shell, the shell nonuniformities are not susceptible to the Rayleigh–Taylor instability during this period. The perturbations, however, grow during this phase due to nonuniform laser illumination (power imbalance, beam mistiming, and single-beam nonuniformities or laser imprint). The initial outer-surface roughness, in general, can be amplified as well by the Richtmyer–Meshkov instability at the ablation front; such a growth, however, is totally stabilized by ablation.[39] As a result, the mode spectrum due to the initial outer-surface roughness does not significantly change during shock transit.

First, the evolution of the long-wavelength modes seeded by the power imbalance among the 60 OMEGA beams is described. This imbalance is due to beam mispointing, different beam shapes, beam mistiming, and energy imbalance among the beams. Beam mistiming results in a temporal shift of each beam and energy imbalance is modeled as an overall height shift of each beam. The tilt that might be introduced to each beam pulse shape is not included in these calculations. The resultant laser illumination amplitudes due to these sources are shown in Fig. 3 for the dominant modes. The perturbation amplitude for a given mode is obtained by overlapping and decomposing the 60-beam energies on a sphere into spherical harmonics. The amplitude of the corresponding Legendre mode is obtained by adding all the m-mode amplitudes in quadrature. The

phase of the mode is chosen to be that of the $m = 0$ spherical harmonic. The large perturbation amplitudes of the Legendre modes correspond to the beginning of the laser pulse and are mainly due to beam mistiming (~12-ps rms). Once the peak intensity is reached, the nonuniformity reaches its asymptotic value corresponding to the energy imbalance in the beams (beam energies of the 60 OMEGA beams from a typical shot are used to apply energy imbalance), beam mispointing (~24-μm rms),[40] and differences in beam shapes (~11-μm rms in super-Gaussian radius and ~0.6% rms in super-Gaussian exponent). These values are typical of OMEGA. The target is assumed to be at the target-chamber center. (Typically on OMEGA, plastic shells are within 5 μm of target chamber center at shot time.) Mode numbers 2 and 4 have the largest amplitudes as indicated by Fig. 3. Mode number 10 is due to the 60-beam OMEGA geometry.

A model that describes the seeding of the ablation surface due to the long-wavelength nonuniformities is described in Appendix A. This sharp-boundary model relates the modal amplitudes at the fuel–shell interface to the modulation in drive pressure, that is in turn related to the modulations in laser intensity using the "cloudy-day" model.[41] Here, the results of this model are compared with the full 2-D simulation involving modes up to 10. The modal amplitudes of the D_2–CH interface at the onset of the acceleration phase are shown in Fig. 4 for the 20-μm-thick implosion. These are obtained by decomposing the interface perturbations from the 2-D simulation into Legendre modes (solid circles). The amplitudes obtained from the model (crosses) are also shown in Fig. 4. The results of the simulation are well reproduced by the simple model.

Next, the evolution of target nonuniformities caused by single-beam modulations (laser imprint) is described. Since laser imprint stays in the linear regime during shock transit, the mode spectrum is calculated by carrying out a series of single-mode, 2-D simulations up to the beginning of the acceleration phase. Imprint simulations are performed by imposing a 1% single-mode modulation in the laser illumination. 1-THz,

2-D SSD[34] is applied to the perturbation amplitudes. SSD is modeled nondeterministically. Each mode is characterized by a coherence time given by $t_c = \left[\Delta\nu \sin\left(n_c \pi \ell / \ell_{\max}\right)\right]^{-1}$, where $\ell_{\max} = 2\pi R_0/\delta$ is the mode number corresponding to half the speckle size δ (δ = 2.35 μm for the OMEGA system), R_0 is the initial outer shell radius, $\Delta\nu$ is the SSD bandwidth, and n_c is the number of color cycles on the laser system. The phase of the mode is chosen randomly every coherence time (the "flipping" approximation). This scheme mimics the average response of the target to the laser modulations. Averaged over time T, the single-beam rms nonuniformity, for a constant-intensity laser pulse, decreases as $\sqrt{t_c/T}$. For each mode in the simulation, the sequence of phases corresponds to a discrete two-state random walk. The number of the statistically independent phase sequences is limited by a finite maximum angular spread $\Delta\theta$ of the light propagating through the laser. The averaged mode amplitude cannot be reduced by SSD to levels below the asymptotic limit. This limit is inversely proportional to the square root of the number of statistically independent speckle patterns $N_{\text{stat}}(\lambda) = \left(4S^x_{\max}/\lambda\right)\left(4S^y_{\max}/\lambda\right)$, where $\lambda = 2\pi R_0/\ell$ is the nonuniformity wavelength, $S^{x(y)}_{\max} = F\Delta\theta^{x(y)}$ is the maximum spatial shift in the x(y) direction, F = 180 cm is the focal length, and $\Delta\theta^x$ = 50 μrad and $\Delta\theta^y$ = 100 μrad for the OMEGA laser system. The asymptotic limits are modeled in the flipping approximation by selecting only N_{stat} independent choices for the sign of the nonuniformity amplitude. The average over a large number of runs will then correspond to the expected response of the target to the single mode. The calculated ablation-front amplitude at the beginning of the acceleration phase η_{0} is a decaying function of the mode number ℓ.[42] This is due to both the shorter decoupling time and the stronger dynamic overpressure stabilization of the higher-ℓ modes. When the effect of SSD is included, the imprint efficiency scales linearly with the mode wavelength. For the plastic shells driven by a 1-ns square pulse with 1-THz, 2-D SSD, the numerical calculations give the following ablation-front amplitude per 1% laser nonuniformity:

$$\eta_{\%} \simeq 6\times10^{-5}\left(6.7+2\pi R_0/\ell\right), \tag{1}$$

where the initial shell radius R_0 and $\eta_{\%}$ are in microns. To calculate the mode spectrum at the ablation front due to the laser imprint, amplitude $\eta_{\%}$ is multiplied by σ_{rms} of the laser nonuniformity of a particular mode.

Calculation of the laser $\sigma_{\text{rms}}(\ell)$ includes the effects of the distributed phase plates (DPP's) used on the beams.[36–38] Laser beams are phase converted by being passed through the DPP's on the OMEGA laser. The DPP's improve the focused single-beam uniformity by removing the large-scale beam structure that has a higher imprint efficiency [see Eq. (1)], leaving intensity profiles with a well-controlled envelope modulated by fine-scale speckle with a lower imprint efficiency. An analytical model that describes this fine speckle[43] is used to model the static single-beam nonuniformity in 2-D simulations in which the ℓ-mode nonuniformity is given as

$$\sigma_{\text{rms}}^2\left(\ell\right)=\frac{16\ell}{\pi\ell_{\text{max}}^2}\left[\cos^{-1}\left(\frac{\ell}{\ell_{\text{max}}}\right)-\frac{\ell}{\ell_{\text{max}}}\sqrt{1-\left(\frac{\ell}{\ell_{\text{max}}}\right)^2}\right]. \tag{2}$$

This mode spectrum was confirmed experimentally in Ref. 44. The illumination nonuniformity given by Eq. (2) is shown in Fig. 5 as a function of mode number. Note that the laser nonuniformity amplitudes initially increase as a function of mode number (up to $\ell \sim 600$), opposite to the decay in the imprint efficiency with the wave number [Eq. (1)].

Polarization smoothing reduces the amplitude by a factor of $\sqrt{2}$.[35] Further reduction in modal amplitudes is obtained with beam overlap. This reduction factor is

obtained by comparing the result of overlapping 60 OMEGA beams on a sphere with the single-beam DPP amplitudes. A reduction factor of $\sqrt{12}$ reproduces the resultant overlapped amplitude pattern on a sphere. Overall amplitudes in the *DRACO* simulation are correspondingly reduced. The resulting imprint spectrum (dashed line) at the ablation front is plotted in Fig. 6. The ablation-surface amplitude due to imprint from one multimode *DRACO* simulation up to mode number 200 (solid line) is shown in Fig. 6 for comparison. The multimode simulation shows variations in the imprint spectrum due to the nondeterministic scheme used to model SSD. Good agreement, on average, between two calculations confirms the linear behavior of imprint prior to shell acceleration.

We compare the seeding due to all three nonuniformity sources in Figs. 6 and 7. The contribution of the ablation-surface nonuniformity from power imbalance and surface roughness[45] is shown in Fig. 7. The comparison of this spectrum with Fig. 6 shows that the main contribution to the low-ℓ modes comes from beam imbalances. Surface roughness has a smaller contribution at low ℓ. Laser imprint (Fig. 6) dominates the intermediate ($10 < \ell < 50$)- and high-ℓ-mode seeding (comparison not shown).

B. Acceleration phase

The two main sources of perturbation growth during the acceleration phase are (1) the RT instability caused by the opposite directions of the pressure and density gradients at the ablation front and (2) the secular growth due to the asymmetries in the laser drive. The latter growth is important only for low-ℓ modes where the wavelength is much longer than the distance between the laser deposition region and the ablation front (conduction zone). Shorter-wavelength drive nonuniformities are smoothed out by the thermal conduction in the conduction zone (the cloudy-day effect). In addition, the RT growth rate increases with mode number; therefore, secular growth becomes negligible at the shorter wavelengths.

The relative importance of the secular growth versus the RT growth for different long-wavelength modes is illustrated in Appendix B using a simple model. The model indicates that the final amplitudes at the end of the acceleration phase due to growth alone are significantly smaller than when RT growth is also included for long-wavelength nonuniformities. This suggests that power balance is extremely important during the period of shock transit when the seeds for RT growth are established. During the acceleration phase, beam imbalances are less important because the resulting growth is dominated by RT growth. This is confirmed by the results of the simulations shown in Fig. 8. In simulation 1 (solid line), beam imbalance is turned off at the start of acceleration, whereas in simulation 2 (dotted line), it is retained throughout the laser pulse. The ablation-surface amplitudes vary by less than 20%, confirming that beam balance is important primarily during shock transit phase only. Since beam mistiming dominates among the various sources of beam imbalances during the shock transit phase, this suggests that beam mistiming provides the largest seed for long wavelength nonuniformities on target.

Next, evolution of the intermediate ($10 < \ell < 50$)- and short-wavelength modes ($\ell > 50$) is considered. Single-beam nonuniformity (laser imprint) provides the main seed for these modes. The initial spectrum of imprint perturbations at the ablation surface is peaked at the low-ℓ modes (Fig. 6). The RT growth rate, however, increases with the mode number, shifting the spectral maximum during acceleration toward shorter wavelengths. Mass ablation significantly reduces RT growth rate compared to the classical limit.[11–13] As shown in Ref. 46, a rather complicated expression for the growth rate can be fit with much simpler formulae:

$$\gamma = \alpha_1 \sqrt{kg} - \beta_1 k V_a, \quad Fr >> 1, \tag{3}$$

$$\gamma = \alpha_2 \sqrt{\frac{kg}{1+kL_m}} - \beta_2 k V_a, \quad Fr << 1, \tag{4}$$

where $Fr = V_a^2 / (gL_0)$ is the Froude number, L_0 is the characteristic thickness of the ablation front, L_m is the minimum density-gradient scale length, and V_a is the ablation velocity defined as the mass ablation rate divided by the shell density. The coefficients $\alpha_{1,2}$ and $\beta_{1,2}$ are functions of the Froude number and the effective power index for thermal conduction ν. The dispersion formulae described in Eqs. (3) and (4) have been verified experimentally in Ref. 47 for CH. For the 20-μm-thick plastic shell considered in this paper, the time-averaged acceleration, ablation velocity, ablation-front thickness, and power index, respectively, are g = 320 μm/ns^2, V_a = 3.2 μm/ns, L_0 = 0.18 μm, L_m = 0.72 μm, and ν = 1; therefore, the Froude number is small, Fr = 0.18, and Eq. (4) can be used to calculated the RT growth rate. The fitting procedure described in Ref. 45 gives the following coefficients: α_2 = 0.94 and β_2 = 1.50. Growth rates from single-mode simulations (solid circles in Fig. 9) compare very well with this analytic formula (dotted line in Fig. 9). Each simulation point in Fig. 9 is a single-mode simulation with a small amplitude perturbation to the laser nonuniformity, such that the mode growth remains in the linear regime during the acceleration. Equation (4) also indicates that the cutoff (modes beyond the cutoff are totally stabilized by ablation) occurs at very high ℓ modes, ℓ_c = 1220, and the growth rate does not decrease significantly even for mode numbers as high as $\ell \sim 600$ for these plastic ablators. Modes above $\ell \sim 600$, however, have a much smaller initial amplitude and experience nonlinear saturation. Their contribution to the total nonuniformity budget is therefore insignificant.

Radiation plays a stabilizing role during the acceleration phase. Absorption of the emission from the corona by the shell raises the shell adiabat near the ablation front, leading to adiabat shaping by radiation in the shell. This increases the ablation velocity

(from ~2.2 μm/ns to ~3.2 μm/ns) and the density-gradient scale length (from L_m = 0.1 μm to 0.7 μm). Since the density-gradient-scale-length is much shorter when the radiation transport is turned off, the Froude number increases, Fr = 0.7 (compare to Fr = 0.18 with radiation). Fitting the growth rate gives the following result: $\gamma_{\mathrm{NoRad}} = 0.92\sqrt{kg/(1+kL_m)} - 1.59\ kV_a$. The cutoff mode number in this case increases from ℓ_c = 1200 to ℓ_c = 4000, and the growth rate of mode ℓ = 200 increases from γ = 7.8 ns^{-1} to 10.1 ns^{-1}. The growth rates for the cases with and without radiation transport are summarized in Fig. 9.

Ablation surface amplitudes at the end of the acceleration phase from single-mode simulations using the realistic imprint amplitudes due to the use of phase plates are shown in Fig. 10. SSD and polarization smoothing are applied to smooth the nonuniformity over time. Since beam smoothing is modeled nondeterministically, the average of several simulations is used for the ablation surface amplitude. Each simulation point in Fig. 10 is the ablation-surface amplitude obtained from the average of five simulations with the error bar representing the standard deviation of these five simulations. It can be seen that modes up to at least 400 contribute to the ablation-surface nonuniformity. A full 2-D simulation would require, therefore, at least 400 modes to realistically model the shell stability during the acceleration phase.

The more-massive 27-μm-thick plastic shell accelerates less (g = 240 μm/ns^2) and consequently has lower RT-growth rates. The nonuniformity seeds at the end of the acceleration phase from feedthrough are, therefore, also smaller at the D_2–CH interface.

C. Coasting phase

Shortly after the laser drive is turned off, the shell stops accelerating and starts to coast with a constant spatially averaged velocity. The coasting phase lasts until the main shock reflects from the center and begins to interact with the incoming shell. Even though the shell perturbations are not subject to the RT instability while the shell coasts inward,

the perturbations are amplified by Bell–Plesset growth. This growth is due to convergence and scales approximately as $\eta \sim (\rho r^2)^{-1}$. Since the shell coasts inward, the shell radius decreases and the perturbation amplitude grows. Furthermore, both the front and back surfaces of the shell and the D_2–CH interface expand (in the frame of reference moving with the shell) with the local sound speed, leading to a decrease in the density that further amplifies the perturbations. In general, the equation governing the perturbation evolution in the absence of acceleration has a weak mode-number dependence.[33] Simulations, however, show a strong ℓ-dependence of the Bell–Plesset growth, especially for long- and intermediate-wavelength modes (see Fig. 11). This dependence is due to the differences in long- and short-wavelength growth prior to the coasting phase. Since the low-ℓ RT growth rate scales as a square root of the mode number ℓ (ablative effects are insignificant), the longer-wavelength perturbations have lower RT growth rates during the shell acceleration. Therefore, at the end of the pulse, the velocity perturbation at the D_2–CH interface is proportional to the square root of the mode number. To illustrate how mode dependence appears in the convergence growth, a simple model for the perturbation evolution during the coasting phase is:[15]

$$\frac{d}{dt}\left[\frac{d\left(\rho r^2 \eta\right)}{dt}\frac{1}{\rho r}\right] = 0. \tag{5}$$

Integrating Eq. (5) twice with the initial conditions $\eta(t=0) = \eta_0$ and $d\eta/dt(t=0) = \eta_0' \simeq \sqrt{\ell/R_0 g}\,\eta_0$ gives the perturbation growth factor

$$\frac{\eta}{\eta_0} = C_c^2\left[\frac{\rho_0}{\rho} + \left(-\frac{2V_{\text{imp}}}{\rho R_0^2} + \sqrt{\frac{\ell g}{R_0}}\frac{1}{\rho R_0}\right)\int_0^t \rho(t')\, r(t')\, dt\right], \tag{6}$$

where C_c is the shell convergence ratio during the coasting phase, R_0 is the shell radius at the end of the acceleration phase, ρ_0 is the density at the end of the acceleration phase, and V_{imp} is the implosion velocity. Equation (6) shows that the longer-wavelength modes experience smaller growth factors, in agreement with the results of simulations (see Fig. 11). The behavior of shorter wavelengths ($\ell > 50$), however, is different from Eq. (6). The perturbations at the D_2–CH interface for such modes decouple from the unstable ablation front during shell acceleration when $\Delta_{int}\ell/r$ becomes greater than unity, where Δ_{int} is the distance between the ablation front and the interface. After decoupling, the interface perturbations start to oscillate with increasing amplitude due to the convergence effects. The growth factor for such modes is defined as the ratio of the interface amplitude at the end of shell coasting to the amplitude maximum during the acceleration phase. Then, $\eta_0' \neq \sqrt{\ell/rg}\eta_0$ and ℓ-dependence of the solution of Eq. (5) becomes much weaker than $\sqrt{\ell}$. This is confirmed in Fig. 11, that shows a clear saturation of the growth factors after $\ell \sim 30$ for the 27-μm-thick implosion. The lines in Fig. 11 are a $\sqrt{\ell}$ fit to growth factors for ℓ <30. For the 20-μm-thick implosion, this saturation is less apparent. The 27-μm shell moves slower during the acceleration phase; hence, it coasts for a longer time (C_c = 2.2 for 20-μm shell and C_c = 3.0 for 27-μm shell). This leads to larger coasting-phase growth factors in thicker shells. It is important to note that the larger D_2–CH growth factors during coasting partially compensate for the smaller nonuniformity seeds at the start of the coasting phase for the thicker, 27-μm implosion. At shell stagnation, therefore, the interface distortions would exhibit very little sensitivity to shell thickness for these two implosions. However, as will be shown in Sec. V, a significant difference in shell stability arising from shorter wavelength growth during the acceleration phase results in very different compressions for these implosions.

D. Deceleration phase

The coasting phase is followed by shell deceleration when the main shock reflected from the center begins to propagate outward inside the shell. The shell is defined as the high-density portion of the CH material (according to a standard definition, the shell is bounded by the $\rho_{\max}/e$ points on both sides from the position of the maximum density $\rho_{\max}$, also Fig. 12). The fuel, together with the inner lower-density, high-temperature CH, forms the hot spot. As the shell converges and temperature inside the hot spot increases, the heat front advances outward and ablates the colder portion of the shell. Therefore, the mass of the higher-temperature hot spot increases during the deceleration phase. This is similar to the hot-spot formation in cryogenic ignition designs.[48] The main difference between cryogenic implosions and the gas-filled plastic implosions is that the hot spot in a cryogenic target consists only of the fuel, while the plastic implosions have two materials—fuel and CH. Since there is a mismatch in the average ion charge Z of the two materials, the density and thermal conductivity are discontinuous across the material interface. The density jump is easily obtained from the pressure continuity condition across the interface in the absence of radiative effects. The total pressure of the ionized gas is $p = \rho T/A$, where T is the temperature, $A = m_i/(1+Z)$, and m_i is the average ion mass. Since the heat flux is continuous across the interface, the temperature must be continuous as well; therefore, the jump in density becomes

$$\frac{\rho_{\mathrm{CH}}}{\rho_{\mathrm{DD}}} = \frac{m_{\mathrm{CH}}}{m_{\mathrm{DD}}}\frac{1+Z_{\mathrm{DD}}}{1+Z_{\mathrm{CH}}}. \tag{7}$$

Substituting $m_{\mathrm{CH}} = 6.5\ m_p$, $m_{\mathrm{DD}} = 2m_p$, $Z_{\mathrm{CH}} = 3.5$ and $Z_{\mathrm{DD}} = 1$ into Eq. (7) gives $\rho_{\mathrm{CH}}/\rho_{\mathrm{DD}} = 1.44$, which leads to the Atwood number $A_T = 0.18$. Here, m_p is the proton mass. Such a density jump across the material interface creates conditions for the RT

growth. There are two RT unstable regions during the deceleration phase: (1) the classically unstable CH–D_2 interface with A_T = 0.18 and (2) the rear surface of the shell. Density profiles at peak neutron production are shown in Fig. 12 to illustrate this point. The simulation without radiative effects (solid) shows two distinct regions of instability: the fuel–shell interface with an Atwood number of 0.18 and a less-steep density gradient leading up to the peak density. While the first region is unstable for all mode numbers, the growth rate at the second region is significantly reduced by the density-gradient scale length and mass ablation. With radiative effects included in the calculation (dotted), however, the effective Atwood number at the interface significantly increases to ~0.5 from the relatively small value of 0.18. This effect is due to the ablation of the colder shell material. As the shell material ablates and is heated by the thermal conduction from the core, the bremsstrahlung radiation increases. The radiation losses lead to additional cooling and compression of the blowoff CH. The simulation with radiation transport in Fig. 12 (dotted line), at peak neutron production, has a larger A_T compared to the simulation without radiation (solid line). As a consequence of this increased Atwood number, there is an increase in the RT instability growth rate for long and intermediate wavelengths. The RT instability creates a lateral flow of the fuel along the interface that moves the fuel from the hotter spike region into the colder bubbles. This leads to an effective cooling of the fuel and degradation in the neutron production rate. Such a mechanism of the neutron-yield truncation is dominant for the thicker shell, which is stable enough during the acceleration phase to maintain its integrity.

As mentioned earlier, the main shock reflected from the target center starts to propagate across the shell at the beginning of the deceleration phase. The material behind the shock stagnates, transferring the shell's kinetic energy into the internal energy of the hot spot. The larger momentum flux of the shell material across the shock results in higher hot-spot stagnation pressure. To estimate the dependence of the final hot-spot pressure P_f on the shell's parameters, we use the continuity conditions across the shock

propagating inside the shell, which moves with implosion velocity $V_{\rm imp}$ and has density $\rho_{\rm sh}$. In the shock-front frame of reference, the mass-flow continuity gives

$$\rho_c U_2 = \rho_{\rm sh} U_1, \tag{8}$$

where U_1 and U_2 are the fluid velocities ahead and behind the shock and ρ_c is the compressed density behind the shock. Since the material behind the shock stagnates in the laboratory frame of reference, $U_2 = U_s$ and $U_1 = V_{\rm imp} + U_s$, where

$$U_s \simeq \sqrt{\frac{\gamma+1}{2}\frac{P_f}{\rho_{\rm sh}}} \tag{9}$$

is the shock velocity in the strong-shock limit and $\gamma = 5/3$ is the ratio of specific heats. Combining Eqs. (8) and (9) and using $\rho_c \simeq 4\rho_{\rm sh}$ gives

$$P_f \sim \rho_{\rm sh} V_{\rm imp}^2 \sim \frac{E_{\rm kin}}{R_{\rm hs}^2 \Delta_{\rm sh}}. \tag{10}$$

At shell stagnation, the kinetic energy of the shell $E_{\rm kin} = M_{\rm sh} V_{\rm imp}^2 \big/ 2$ is transferred into the internal energy of the hot spot $2/3\, P_f R_{\rm hs}^3$. Substituting this latter expression for the kinetic energy into Eq. (10), one sees that the stagnation radius is proportional to the shell thickness $R_{\rm hs} \sim \Delta_{\rm sh}$; therefore, the final pressure of the compressed fuel is larger for a "compact" shell with higher density and smaller shell thickness for a given shell kinetic energy. In other words, the kinetic energy of the converging shell heats the hot spot more efficiently in shells with larger compressibility (smaller entropy). Comparing 20- and

27-μm shells, we conclude that the stagnation radius of the thicker shell is larger; thus the final pressure and the neutron-production rate are expected to be smaller. On the other hand, if one compares the shell that remains integral during the acceleration phase with a shell whose stability is severely compromised by RT growth, the integral shell has a lower entropy and smaller shell thickness. It, therefore, stagnates at a smaller radius reaching a higher hot-spot pressure and temperature. This leads to a larger neutron-production rate in the integral shell in comparison with the significantly distorted shell.

The larger shell thickness in the implosion with compromised shell integrity also implies that the rate at which neutron production decreases should be less steep during shell disassembly. Between the time of peak neutron production and peak compression, the neutron rate decreases due to the falling temperature in the gas. The subsequent decrease in the neutron-production rate occurs due to shell disassembly. If the shell is thicker, disassembly occurs later in the implosion as follows: The time between the interaction of the reflected shock (which is very similar for both integral and severely distorted shells) and when the shock breaks out of the shell is given by $t_s = \Delta_{sh}/U_s$. From Eqs. (9) and (10), $U \simeq \sqrt{E_{kin}/R_{hs}^2 \Delta_{sh} \rho_{sh}}$. Since E_{kin} is very similar between the integral shell and severely distorted shell implosion (only a small portion of the total energy goes into lateral flow in the distorted shell implosion) and mass $\left(\propto R_{hs}^2 \Delta_{sh} \rho_{sh}\right)$ is conserved, the shock velocity is very similar in both cases; therefore, $t_s \propto \Delta_{sh}$ and is longer for the thicker shell, and disassembly is delayed. Consequently, neutron production falls less steeply in the implosion where shell stability is compromised than in the implosion with an integral shell.

V. Multimode Simulations

A. Effects of beam-to-beam imbalances

This section describes multimode simulations. As mentioned in Sec. IV(A), imbalances among the beams result in long-wavelength modes on target. Even modes

between 2 and 10 are used to simulate the effect of low-order modes using the amplitudes in Fig. 3. The power in odd modes is added in quadrature to the even-mode amplitudes. Figure 13 shows the fuel–shell interface amplitudes versus time for the dominant modes in the simulation for the 20-μm-thick shell implosion. The initially unperturbed interface acquires a perturbation shortly after shock breakout around 0.4 ns. When the compression wave returns to the interface, it causes another jump in the perturbation around 0.8 ns. Significant growth is simulated after this time due to the feedthrough of the perturbation from the ablation surface and the convergent Richtmyer–Meshkov instability. Modes 6 and greater start oscillating shortly after the end of the acceleration phase as they decouple from the ablation surface. The reflected shock from the center returns to the interface around 1.75 ns, when $\ell = 4$ changes phase. Rayleigh–Taylor growth occurs shortly after that as the shell continuously decelerates toward stagnation.

The yield is only marginally affected by low-order modes with 2-D simulation resulting in ~95% of the 1-D yield for the 20-μm-thick shell and ~94% of 1-D for the 27-μm-thick shell. Figure 14 shows the density contour at peak neutron production for the 20-μm-thick implosion. The D_2–CH interface is marginally distorted. The areal density variations are ~23% at peak neutron production (for both shell thicknesses). To account for other sources of nonuniformity that are not included in the calculations, the initial beam imbalance is multiplied by a factor of 2. This results in a yield relative to 1-D of ~90% for both thicknesses.

The marginal effect of low-order modes is consistent with the beam-balancing experiment described in Ref. 36. In that work, on-target beam balance was changed in a controlled manner; the estimated decrease in the amplitude of these modes was between 30%–50%. While a decrease in areal-density variations was observed, only a marginal difference in absolute neutron yields was observed.

B. Effects of single-beam nonuniformity

Single-beam nonuniformity seed intermediate- and short-wavelength modes on target. As mentioned earlier, modes up to at least 400 are required to realistically model shell stability. A full 2-D simulation including the effects of power imbalance would then require modes between 2 and 400. Resolving mode 400 in such a simulation requires a large number of computational zones—far beyond the scope of this work. We illustrate the effect of laser imprint on shell stability by performing simulations with a smaller set of modes. The simulations include beam-smoothing techniques described in Sec. IV(B). Figure 15(a) shows a plot of density contours at the end of the acceleration phase from a simulation that includes even modes up to $\ell = 200$ for the 20-μm-thick CH shell. The shortest wavelength in this simulation is resolved using 14 cells, resulting in a 200×700 zone simulation. Since odd modes are not included in the simulation, their power is added in quadrature to the amplitudes of the even modes. The shell indicated by the high-density regions is considerably distorted with portions of the shell at less than solid densities. The peak-to-valley variation in the center-of-mass radius is calculated to be 6.6 μm at the end of the acceleration phase, significantly greater than the 1-D shell thickness of ~5 μm. It is expected that the shell distortion will only increase when even-shorter wavelengths are included in the calculation. Therefore, short wavelengths play an important role in increasing the adiabat of the shell by introducing additional degrees of freedom for the fluid flow. This will influence the compressibility of the shell and, therefore, neutron yields. In comparison, the 27-μm-thick implosion [Fig. 15(b)] has an integral shell at the end of the acceleration phase with a peak-to-valley amplitude of 3.4 μm in the center-of-mass radius compared to a shell thickness of ~6.8 μm. The effect of the still-shorter wavelengths not included in the calculation ($\ell > 200$) can be estimated using a RT postprocessor[33] to the 1-D simulation. This postprocessor indicates that the thicker, 27-μm-thick shell remains integral during the acceleration phase while the stability of the 20-μm-thick shell is severely compromised.

Due to the large number of computational cells in these simulations, it is extremely challenging to reliably simulate these implosions through peak compression. Instead, the effect of the various nonuniformity sources are assessed as follows:

Simulations that include only a few modes represent shell stability reasonably well. The goal of these simulations is to identify the mechanisms that influence neutron yields. More detailed comparisons with experimental observables will be performed in the future.

VI. Combined Effects of All Sources of Nonuniformity

Simulations that include a few modes are useful to shed light on which modes influence target performance. The mode ranges are divided into three regions: long wavelengths ($\ell \leq 10$), intermediate wavelengths ($10 \leq \ell \leq 50$), and shorter wavelengths that include all the higher mode numbers. In Sec. V(A), it has been pointed out that low-order modes ($\ell \leq 10$) alone have a marginal influence on target performance. 2-mode simulations corresponding to mode numbers 4 and 20 that combine the effect of long and intermediate wavelengths are performed. These simulations and those described later are performed on a 45° wedge. The initial amplitude for each mode is chosen from the amplitudes added in quadrature of a range of mode numbers (from the DPP and PS spectrum for $\ell = 20$ using modes between 15 and 40 as the mode range and from the initial power balance and surface-roughness data for modes $2 < \ell < 8$ for mode $\ell = 4$). The neutron-production rate is shown in Fig. 16(a) for the 20-μm-thick implosion and Fig. 16(b) for the 27-μm-thick implosions. The rate from the two mode simulations (dotted line) deviates from the 1-D simulation, and the burn truncates relative to 1-D. This is the case for both thicknesses. The two-mode simulation illustrates the mechanisms for yield reduction through burn truncation. The RT and RM growth at the fuel–shell interface results in the flow of fuel into the colder bubbles, decreasing the yield. This is illustrated in Fig. 17, where the fluid velocity vectors (arrows) in the frame

moving radially in with the fluid are overlaid on the contour plot of ion temperature at peak neutron production. This result is shown from a single-mode simulation of mode number 20, where this mode has the same initial amplitude as the previous two-mode simulation. Due to heat conduction, the temperature contours are more spherically symmetric than the material interface (solid line). As the vectors indicate, fuel flows into the colder bubbles. This truncates the neutron-production rate. The second truncation mechanism is due to the distortion of the high-density shell. The increased surface area enhances heat conduction out of the core, cooling the fuel and decreasing the yield. These truncation mechanisms cannot be included in 1-D mix models that have been used previously to model these implosions.[6,8,49] The single intermediate-mode simulation has a yield relative to 1-D of 78% (for both thicknesses). The addition of long wavelengths ($\ell = 4$) reduces this value to 55% for the 20-μm-thick shell and 61% for the 27-μm-thick shell. Thus, the combination of the low and intermediate modes has a greater effect on yield than each range of modes alone.

To investigate the role of the shorter wavelengths on yield, three-mode simulation including mode numbers 4, 20, and 200 are performed. In this simulation, modes 4 and 20 have the same amplitude as the simulation discussed earlier. The amplitude for mode $\ell = 200$ is chosen by adding in quadrature the power between modes 100 and 300. Contours of mass density for the two shell thicknesses are shown at peak neutron production in Fig. 18. The significant shell distortion corresponds to the intermediate mode, $\ell = 20$. Even though the growth rate at the D_2–CH interface is highly nonlinear for the short wavelength ($\ell = 200$), the bubble amplitude is, at most, 1 μm. This amplitude can be physically explained as follows: since a hydrodynamic code such as *DRACO* cannot follow materials into the turbulent regime, we consider the amplitude of the short wavelength as a "mix thickness." The simulated thickness is consistent with expectations from turbulent mixing. The turbulent mixing layer grows self-similarly with a mixing thickness h, given by Ref. 50

$$h = \alpha A_T g t^2, \tag{11}$$

where α is a dimensionless constant.

As described in Sec. IV(D), bremsstrahlung cooling increases CH density in the hot spot. Consequently, the Atwood number varies continuously during the deceleration phase, reaching a maximum value of 0.5. The increased density, however, does not significantly alter the short wavelength perturbation growth rate due to the stabilizing effects of the density-gradient scale length and thermal conduction. Taking $A_T = 0.18$ for the D_2–CH interface gives $\alpha = 0.05$ (Ref. 50). This leads to $h = 0.9$ μm. This compares favorably with the amplitude of $\ell = 200$ inferred from simulation. In previous work, homogenous mixing of D_2 and CH[6–8,49] has been inferred from experimental observables such as secondary neutron ratios,[6,8] argon spectral lines,[7] D^3He yields in ^3He-filled CD shells,[6,8] etc. Primary neutron yields have not been directly used to determine the presence of turbulence. Larger mixing widths (~20 μm) have been inferred based on spherically symmetric 1-D mix models. Since 1-D mix models need to account for the increased volume due to long wavelength distortions, it is very likely that they overestimate the mixing length. The relatively small turbulent mixing layer (compared to the overall deformation of the interface due to intermediate mode numbers) suggests that the experimentally inferred turbulence plays a small role in determining primary neutron yields, but likely influences the other observables mentioned above.

The simulations including $\ell = 200$ also indicate an interesting trend in neutron production when compared to the simulations including only low and intermediate modes (Fig. 16). For both shell thicknesses, the peak in the neutron-production rate deviates earlier from 1-D simulations. For the 20-μm-thick shell, however, neutron production does not decrease as steeply as the previous two-mode simulation. For the 27-μm-thick

shell, the neutron-production history is very similar in width to the two-mode simulation. This difference in trends can be explained as follows: The shell is integral for the 27-μm-thick shell and the density and temperature distribution compare favorably with 1-D [this is shown in Fig. 19(b)]. The solid black line is the 1-D result, whereas the other two lines correspond to radial lineouts from the simulations (dashed at 36° and dotted at 0°). For the 20-μm-thick shell, the profiles from the 2-D simulation are significantly different from 1-D [Fig. 19(a)]. The peak densities are much lower, and the shell has a wider extent due to the increased adiabat from shell breakup during acceleration. This profile results in delayed stagnation as the shock takes much longer to reach the back of the shell [see Sec. IV(D)]. This delayed shell disassembly results in a persistence of neutron production compared to the simulation including only low and intermediate modes. Figures 19(c) and 19(d) show the corresponding radial temperature lineouts from the simulation. The lower temperature in the 27-μm implosion [Fig. 19(d)] is due to the shell distortion and increased heat flow from the core. The 20-μm implosion [Fig. 19(c)], in addition, shows lower temperature due to the decreased compression. The yields relative to 1-D are 21% for the 20-μm-thick CH shell compared to 47% for the 27-μm-thick CH shell. Experimentally, the yields relative to 1-D are ~40% and ~45% for the 20-μm and 27-μm thicknesses, respectively. Since mode ℓ = 200 has a larger effect on the 20-μm implosion, the smaller yield relative to 1-D in the simulation for the 20-μm implosion points to an overestimate of the initial amplitude of ℓ = 200 in the simulation.

Similar trends in neutron-production rates are observed in experiments. Figure 20 shows the neutron-production rates from experiment (solid line), the 1-D simulation (dotted line), for the 20-μm-thick implosion [Fig. 18(a)] and the 27-μm-thick implosion [Fig. 18(b)]. Since absolute timing in these experiments was unknown, the 1-D rates are overlaid on the experimental rates by aligning the rise times of the two neutron rate curves. For the thinner shell, the experimental burnwidth is closer to 1-D, whereas for the thicker, more-stable shell, the burnwidth is truncated compared to 1-D. This trend

persists: a still thicker shell (33 μm) shows increased burn truncation, and even thinner shells (15-μm) indicate a widening of the neutron-production history. The 2-D simulation of the 20-μm implosion shows a slower fall of the neutron-production rate compared to the experimentally observed rate. This is likely due to the larger value for the initial amplitude of the $\ell = 200$ mode in the simulation compared to that in experiment.

In summary, the combination of intermediate and low modes significantly influences predicted neutron yields. This is manifest as burn truncation in the neutron-production rates. The short wavelengths significantly affect shell stability for the thinner shells and influence stagnation. This widens the burnwidth and also influences yields. For the thicker shells, the burnwidth does not change significantly with the addition of short-wavelength modes. In both cases, the neutron rates deviate earlier from 1-D with the addition of short wavelengths in simulation.

VII. Conclusions

One-dimensional dynamics of high-adiabat plastic-shell implosions of two different thicknesses irradiated by a smooth laser were discussed. Seeding and evolution of nonuniformities was discussed for the different phases of the implosion. During the acceleration phase, modes up to at least ~400 should contribute to shell stability. Multimode simulations using the code *DRACO* indicate that the shell stability in the implosion of a 20-μm-thick plastic shell is significantly compromised due to the Rayleigh–Taylor instability during the acceleration phase, whereas the 27-μm-thick shell is only marginally distorted. Long-wavelength multimode simulations indicate that imbalances between the laser beams have a small effect on target yields. Intermediate modes appear to influence yields significantly. Short-wavelength modes result in qualitatively different behavior of the neutron production rate between the two shell thicknesses: a slower fall-off compared to 1-D for the thinner shell and marginally influencing burnwidth for the thicker shell. Future work will include detailed

comparisons of charged-particle spectra with experimental observations, an additional analysis to relate small-scale mix thicknesses to observations of homogenous mixing in experiments, and the comparison of x-ray images of the compressed core with experimental observations.

Acknowledgment

This work was supported by the U.S. Department of Energy Office of Inertial Confinement Fusion under Cooperative Agreement No. DE-FC52-92SF19460, the University of Rochester, and the New York State Energy Research and Development Authority. The support of DOE does not constitute an endorsement by DOE of the views expressed in this article. This work has been supported in part by LLE (subcontract PO412163G) with the University of Wisconsin for the implementation of the PetSc Libraries in *DRACO*. Supported in part by DOE at UC, LLNL under W-7405-Eng-48.

APPENDIX A: Seeding of the Long-Wavelength Modes Due to Drive Asymmetry

The nonuniformities in laser intensity results in asymmetries in drive pressure ΔP. To relate the ablation pressure and laser-intensity nonuniformities ΔI, we adopt the "cloudy-day" model.[37] Using the scaling $P \sim I^{2/3}$ yields the following relation:

$$\frac{\Delta P}{P} \simeq \frac{2}{3}\frac{\Delta I}{I} e^{-kD_c} \equiv \frac{2}{3}\tilde{I}, \tag{A-1}$$

where D_c is the size of the conduction zone (the distance between the ablation front and the region of maximum laser energy deposition) and k is the wave number. For the set of experiments described in this paper, the conduction zone grows linearly in time $D_c = V_c t$ with $V_c \simeq 68$ μm/ns. Since the laser intensity is spatially modulated, the shocks driven by

the peaks in the laser illumination travel faster than the shocks launched at the intensity minima; therefore, the shock and ablation fronts get distorted. This distortion growth can be estimated for long-wavelength modes using the following simple model: The shock velocity, in the strong-shock limit, is proportional to the square root of the drive pressure P,

$$U_S \simeq \sqrt{\frac{\gamma+1}{2}\frac{P}{\rho_0}}, \tag{A-2}$$

where ρ_0 is the initial (undriven) shell density and γ is the ratio of specific heats (γ= 5/3 for the monoatomic ideal gas and is used here). Drive pressure modulations distort the shock front according to

$$\frac{d\eta_S}{dt} = \Delta U_S = \frac{dU_S}{dP}\Delta P_S \simeq \frac{2}{\sqrt{5}} c_S \frac{\Delta P}{P}, \tag{A-3}$$

where c_S is the sound speed of the shock-compressed shell, ΔP_S is the pressure modulation at the shock, and η_S is the shock-front amplitude modulation. We approximate ΔP in the latter equation with the modulation at the ablation front [Eq. (A-1)]. This approximation is justified only for the long-wavelength modes when the lateral fluid motion can be neglected. Ablation front distortions are caused by the perturbations in the post-shock velocity $U_{\mathrm{ps}} = -\rho_0/\rho U_S$, where U_{ps} is calculated in the shock frame of reference. Such perturbations are due to (1) modulations in the shock velocity, $-(\rho_0/\rho)\Delta U_S$; (2) modulations $\Delta\rho$ in the shock-compressed density, $(\rho_0/\rho)(\Delta\rho/\rho)U_S$; and (3) modulations in the position of the shock front. It can be shown that the density modulation right behind the shock is small for strong shocks

($\Delta\rho/\rho \sim M_s^{-2}\,\Delta P/P$, where M_s is the shock Mach number) and can be neglected. The resulting modulation in the post-shock velocity takes the form

$$\Delta U_{\rm ps} \simeq \left(\rho_0/\rho - 1\right)\Delta U_s = \frac{3}{4}\Delta U_s. \tag{A-4}$$

Since ablative stabilization and lateral flow can be neglected for the long-wavelength modes, $d\eta_a/dt = \Delta U_{\rm ps}$. Integrating the latter equation gives the ablation-front modulation η_a:

$$\eta_a(t) \simeq \frac{1}{\sqrt{5}}\int_0^t dt' \tilde{I}(t')\, c_s(t'), \quad \eta_s = \frac{4}{3}\eta_a. \tag{A-5}$$

It is also important to determine the modulation in the CH–gas interface $\eta_{\rm int}$ at the beginning of the acceleration phase. The modulation at the interface is seeded by the perturbed shock. As soon as the shock breaks out of the shell, the rear surface starts to expand with the velocity 3 c_s (Ref. 51) with respect to the shock-compressed material. Therefore, the amplitude of the CH–gas interface takes the value $\eta_{\rm int}$ = 3 $c_s\delta t$, where $\delta t = \eta_s/U_s$ is the shock transit time across the modulation amplitude. Using the strong shock limit, one obtains $\eta_{\rm int} 3\sqrt{5}\,\eta_s/4$. Taking into account the relation between η_s and η_a yields $\eta_{\rm int} = \sqrt{5}\eta_a$. As shown in Ref. 52, the gas–CH interface is unstable during the rarefaction-wave (RW) propagation through the shell. Since such a growth is linear in time and proportional to the modulation wave number, there is very little change in the amplitude of the fuel–pusher interface between the shock breakout and the beginning of the acceleration phase. To determine the mode amplitudes at the beginning of the acceleration phase, we integrate Eq. (A-5) using the laser nonuniformity profiles shown

in Fig. 3. The spectrum thus obtained is plotted in Fig. 4 and compared against the results of the full 2-D power-balance simulation. Observe that the simple model reproduces the results of simulations very well. To calculate the initial conditions for the RT growth, in addition to the initial amplitude, we must calculate the perturbed front velocity η_a'. This velocity has two components. The first is given by Eqs. (A-4) and (A-3), and the second is due to the rippled RW breakout at the ablation front. Indeed, when the first shock reaches the rear surface, the RW is launched toward the ablation front. The RW travels with the local sound speed c_s; therefore, if the shock amplitude is η_s, then the rarefaction amplitude becomes $\eta_{\mathrm{rw}} = c_s\left(\eta_s/U_s\right) = \sqrt{5}\eta_s/4$. The phase of the modulation in the rarefaction head is opposite to the phases of the rear-surface and ablation-front perturbations. Upon reaching the ablation front, the RW establishes the pressure gradient, accelerating the front. Since the peaks of the RW break out at the ablation front prior to the valleys, the ablation-front ripple gains an additional velocity perturbation $\delta v = g\delta t$, where g is the acceleration and $\delta t = \eta_{\mathrm{rw}}/c_s = \sqrt{5}/3\left(\eta_a/c_s\right)$. Combining the two contributions, the initial ripple velocity takes the form

$$\frac{d\eta_a}{dt}\left(t_0\right) = \tilde{I}\left(t_0\right)\frac{c_s}{\sqrt{5}} + \frac{\sqrt{5}g}{3c_s}\eta_a\left(t_0\right), \tag{A-6}$$

where t_0 is time at the beginning of acceleration phase. Equations (A-5) and (A-6) show that the ablation-front amplitude changes slope at $t = t_0$. Substituting $g = c_s^2/\left(\gamma\Delta_{\mathrm{sh}}\right)$ into Eq. (A-6) and also approximating $\eta_a\left(t_0\right) \sim \left\langle\tilde{I}\right\rangle_{\mathrm{sh}}\left(c_s/U_{\mathrm{sh}}\right)4\Delta_{\mathrm{sh}}$, we can rewrite Eq. (A-6) as

$$\eta_a'\left(t_0\right) \sim \tilde{I}\left(t_0\right)\frac{c_s}{\sqrt{5}} + \left\langle\tilde{I}\right\rangle_{\mathrm{sh}}\frac{c_s}{\sqrt{5}}. \tag{A-7}$$

The second term in the right-hand side of Eq. (A-7) is proportional to the laser nonuniformity averaged over the shock transit time, $\langle \tilde{I} \rangle_{\rm sh}$. Taking into account that beam mistiming significantly increases $\tilde{I}$ at the beginning of the pulse (during the pulse rise), $\langle \tilde{I} \rangle_{\rm sh}$ becomes much larger than $\tilde{I}(t_0)$ (in most cases by a factor of 5). This conclusion is valid for a large variety of target designs, including the ignition design, since the laser reaches its peak intensity prior to the acceleration phase. One must keep in mind, however, that Eq. (A-6) assumes sharp interfaces of the CH–gas boundary and the ablation front. In reality the radiation preheat relaxes the density at the CH–gas interface prior to the first shock breakout. In addition, the ablation front has a finite thickness. These effects cause deviations of the initial condition from simple estimates [Eqs. (A-5) and (A-7)]. Comparison with the results of 2-D simulations shows that finite interface thickness effects do not significantly modify the perturbation amplitudes (Fig. 4).

APPENDIX B: Growth of Long-Wavelength Modes During the Acceleration Phase

The equation describing the perturbation growth for the long-wavelength modes (neglecting ablation) during the acceleration phase can be written as[33]

$$\frac{d}{dt}\left(\frac{1}{\rho r}\frac{d}{dt}\rho r^2\eta\right) - \ell g\eta = \ell\frac{\Delta P}{\rho} = \ell\frac{2}{3}\frac{\delta I}{I}\left(\frac{r}{r_c}\right)^{\ell} g\Delta_{\rm sh}, \qquad \text{(B-1)}$$

where ΔP is the drive pressure nonuniformity, r is the shell radius, g is the shell acceleration, ρ is the shell density, $\Delta_{\rm sh}$ is the shell thickness, r_c is the position of the average laser-energy deposition surface, and η is the ablation-front modulation amplitude. The factor $(r/r_c)^{\ell}$ is due to the cloudy-day effect. Equation (B-1) is subject to the initial conditions (A-5) and (A-6). The shell thickness is $\Delta_{\rm sh}$ = 5 μm for the 20-μm

shell and Δ_{sh} = 6.8 μm for the 27-μm shell. During this phase of the implosion, the shell density remains approximately constant, so we can cancel ρ in Eq. (B-1). For simplicity constant shell acceleration is assumed, $r = r_0 - gt^2/2$. To compare the relative importance of the RT growth versus the secular growth during the shell acceleration, $\ell g \eta$ is compared with the right-hand side of Eq. (B-1). The lower limit of this term is

$$\min\left(\ell g\eta\right) = \ell g\eta\left(t_0\right) \simeq \ell g \left\langle \tilde{I} \right\rangle_{sh} \frac{\Delta_0}{\sqrt{5}} \frac{c_s}{U_{sh}} = \ell g \Delta_{sh} \left\langle \tilde{I} \right\rangle_{sh}, \tag{B-2}$$

where Δ_{sh} is the in-flight shell thickness (which is approximately one-fourth of the initial thickness Δ_0) and $\left\langle \tilde{I} \right\rangle_{sh}$ is the intensity modulation averaged over the shock propagation time. Comparing the latter expression with the right-hand side of Eq. (B-1), we observe that $\Delta P/\rho << g\eta$ during the acceleration phase. The latter inequality is satisfied for very long wavelengths (ℓ < 10) because $\left\langle \tilde{I} \right\rangle_{sh} >> \tilde{I}\left(t_0\right)$ due to beam mistiming early in the pulse. Shorter wavelengths (ℓ > 10) experience a large attenuation due to thermal smoothing in the conduction zone. Therefore, the right-hand side of Eq. (B-1) is also small for such mode. Thus, we can conclude that the secular growth during the acceleration phase is much smaller than the RT amplification of the initial amplitude and velocity of the ablation-front modulation. This growth can be estimated using the WKB solution of the homogeneous part of Eq. (B-1) with the following initial conditions:

$$\eta_0 = \langle \tilde{I} \rangle_{sh}\, \Delta_{sh}, \quad \eta_0' = \frac{c_s}{\sqrt{5}} \left[\tilde{I}\left(t_0\right) + \langle \tilde{I} \rangle_{sh} \right]. \tag{B-3}$$

Using results of Ref. 33, the solution takes the form

$$\eta_a = C_r^{5/4}\left[\eta_0 \cosh\Psi + \eta_0' \sqrt{\frac{r_0}{(\ell+2)g}} \sinh\Psi\right], \qquad \text{(B-4)}$$

where $\Psi = \sqrt{2(\ell+2)}\arcsin\sqrt{1-C_r^{-1}}$ and C_r is the convergence ratio during the acceleration phase. During the acceleration phase, the convergence ratio of the 20-μm shell and the 27-μm shell is $C_r = r_0/r \simeq 1.7$ and $C_r \simeq 1.4$, respectively, where r_0 = 430 μm is the ablation-front radius at the beginning of the shell acceleration. The dominant role of the RT growth over the secular growth is confirmed by the results of *DRACO* simulation. Figure 8 shows a plot of the perturbation amplitude with full power imbalance (dashed–dotted line) and with the power imbalance turned off (solid line) during the acceleration phase.

References

1. J. Nuckolls, L. Wood, A. Thiessen, and G. Zimmerman, Nature **239**, 139 (1972).
2. C. P. Verdon, Bull. Am. Phys. Soc. **38**, 2010 (1993).
3. M. D. Campbell and W. J. Hogan, Plasma Phys. Control. Fusion **41**, B39 (1999).
4. T. R. Boehly, D. L. Brown, R. S. Craxton, R. L. Keck, J. P. Knauer, J. H. Kelly, T. J. Kessler, S. A. Kumpan, S. J. Loucks, S. A. Letzring, F. J. Marshall, R. L. McCrory, S. F. B. Morse, W. Seka, J. M. Soures, and C. P. Verdon, Opt. Commun. **133**, 495 (1997).
5. D. D. Meyerhofer, J. A. Delettrez, R. Epstein, V. Yu. Glebov, V. N. Goncharov, R. L. Keck, R. L. McCrory, P. W. McKenty, F. J. Marshall, P. B. Radha, S. P. Regan, S. Roberts, W. Seka, S. Skupsky, V. A. Smalyuk, C. Sorce, C. Stoeckl, J. M. Soures, R. P. J. Town, B. Yaakobi, J. D. Zuegel, J. Frenje, C. K. Li, R. D. Petrasso, D. G. Hicks, F. H. Séguin, K. Fletcher, S. Padalino, M. R. Freeman,

N. Izumi, R. Lerche, T. W. Phillips, and T. C. Sangster, Phys. Plasmas **8**, 2251 (2001).

6. P. B. Radha, J. Delettrez, R. Epstein, V. Yu. Glebov, R. Keck, R. L. McCrory, P. McKenty, D. D. Meyerhofer, F. Marshall, S. P. Regan, S. Roberts, T. C. Sangster, W. Seka, S. Skupsky, V. Smalyuk, C. Sorce, C. Stoeckl, J. Soures, R. P. J. Town, B. Yaakobi, J. Frenje, C. K. Li, R. Petrasso, F. Séguin, K. Fletcher, S. Padalino, C. Freeman, N. Izumi, R. Lerche, and T. W. Phillips, Phys. Plasmas **9**, 2208 (2002).
7. S. P. Regan, J. A. Delettrez, V. N. Goncharov, F. J. Marshall, J. M. Soures, V. A. Smalyuk, P. B. Radha, B. Yaakobi, R. Epstein, V. Yu. Glebov, P. A. Jaanimagi, D. D. Meyerhofer, T. C. Sangster, W. Seka, S. Skupsky, C. Stoeckl, D. A. Haynes, Jr., J. A. Frenje, C. K. Li, R. D. Petrasso, and F. H. Séguin, Phys. Rev. Lett. **92**, 185002 (2004).
8. C. K. Li, D. G. Hicks, F. H. Séguin, J. Frenje, R. D. Petrasso, J. M. Soures, P. B. Radha, V. Yu. Glebov, C. Stoeckl, J. P. Knauer, F. J. Marshall, D. D. Meyerhofer, S. Skupsky, S. Roberts, C. Sorce, T. C. Sangster, T. W. Phillips, and M. D. Cable, Rev. Sci. Instrum. **72**, 864 (2001).
9. D. Keller, T. J. B. Collins, J. A. Delettrez, P. W. McKenty, P. B. Radha, B. Whitney, and G. A. Moses, Bull. Am. Phys. Soc. **44**, 37 (1999).
10. Lord Rayleigh, Proc. London Math Soc. **XIV**, 170 (1883); G. Taylor, Proc. R. Soc. London Ser. A **201**, 192 (1950).
11. S. E. Bodner, Phys. Rev. Lett. **33**, 761 (1974).
12. H. Takabe, K. Mima, L. Montierth, and R. L. Morse, Phys. Fluids **28**, 3676 (1985).
13. R. Betti, V. N. Goncharov, R. L. McCrory, P. Sorotokin, and C. P. Verdon, Phys. Plasmas **3**, 2122 (1996).

14. R. D. Richtmyer, Commun. Pure. Appl. Math. **XIII**, 297 (1960); V. A. Andronov, S. M. Bakhrakh, E. E. Meshkov, V. N. Mokhov, V. V. Nikiforov, A. V. Pevnitskii, and A. I. Tolshmyakov, Sov. Phys.-JETP **44**, 424 (1976).

15. G. I. Bell, Los Alamos National Laboratory, Los Alamos, CA, Report LA-1321 (1951).

16. M. S. Plesset, J. Appl. Phys. **25**, 96 (1954); D. L. Book and S. E. Bodner, Phys. Fluids **30**, 367 (1987); See National Technical Information Service Document No. DOE/SF/19460-485 [Laboratory for Laser Energetics LLE Review **94**, 81 (2003)]. Copies may be obtained from the National Technical Information Service, Springfield, VA 22161.

17. M. C. Richardson, G. G. Gregory, R. L. Keck, S. A. Letzring, R. S. Marjoribanks, F. J. Marshall, G. Pien, J. S. Wark, B. Yaakobi, P. D. Goldstone, A. Hauer, G. S. Stradling, F. Ameduri, B. L. Henke, and P. Jaanimagi, in *Laser Interaction and Related Plasma Phenomena*, edited by H. Hora and G. H. Miley (Plenum Press, New York, 1986), Vol. 7, p. 179.

18. A. A. Amsden, H. M. Ruppel, and C. W. Hirt, Los Alamos National Laboratory, Los Alamos, NM, Report LA-8095 (1980).

19. M. L. Wilkins, J. Comput. Phys. **36**, 281 (1980).

20. G. Maenchen and S. Sack, in *Methods in Computational Physics*, edited by B. Alder, S. Fernbach, and M. Rotenberg, Fundamental Methods in Hydrodynamics (Academic Press, New York, 1964), Vol. 3, p. 181.

21. A. M. Winslow, J. Comput. Phys. **2**, 149 (1967); S. Atzeni and A. Guerrieri, Laser Part. Beams **9**, 443 (1991); J. U. Brackbill and J. S. Saltzman, J. Comput. Phys. **46**, 342 (1982).

22. B. van Leer, J. Comput. Phys. **23**, 276 (1977).

23. D. J. Benson, Comput. Methods Appl. Mech. Eng. (Netherlands)
Eur. Phys. J. D **99**, 235 (1992).

24. D. L. Youngs, in *Numerical Methods for Fluid Dynamics*, edited by K. W. Morton and M. J. Baines (Academic Press, London, 1982), p. 273.

25. S. P. Lyon and J. D. Johnson, Los Alamos National Laboratory, Los Alamos, CA, Report LA-UR-92-3407 (1992).

26. A. R. Bell, Rutherford Appleton Laboratory, Chilton, Didcot, Oxon, England, Report RL-80-091 (1980).

27. R. M. More, K. H. Warren, D. A. Young, and G. B. Zimmerman, Phys. Fluids **31**, 3059 (1988).

28. W. F. Huebner, A. L. Merts, N. H. Magee, Jr., and M. F. Argo, Los Alamos National Laboratory, Los Alamos, NM, Report LA-6760-M (1977).

29. S. Balay, W. D. Gropp, L. C. McInnes, and B. F. Smith, in *Modern Software Tools for Scientific Computing*, edited by E. Arge, A. M. Bruaset, and H. P. Langtangen (Birkhäuser, Boston, 1997), Chap. 8, p. 163.

30. MPI Version 1.2 Standard for IRIX−A communication language for parallel processing (2001).

31. L. M. Hively, Nucl. Fusion **17**, 873 (1977).

32. R. L. McCrory and C. P. Verdon, in *Inertial Confinement Fusion*, edited by A. Caruso and E. Sindoni (Editrice Compositori, Bologna, Italy, 1989), p. 83.

33. V. N. Goncharov, P. McKenty, S. Skupsky, R. Betti, R. L. McCrory, and C. Cherfils-Clérouin, Phys. Plasmas **7**, 5118 (2000).

34. S. Skupsky, R. W. Short, T. Kessler, R. S. Craxton, S. Letzring, and J. M. Soures, J. Appl. Phys. **66**, 3456 (1989).

35. T. R. Boehly, V. A. Smalyuk, D. D. Meyerhofer, J. P. Knauer, D. K. Bradley, R. S. Craxton, M. J. Guardalben, S. Skupsky, and T. J. Kessler, J. Appl. Phys. **85**, 3444 (1999).

36. C. B. Burckhardt, Appl. Opt. **9**, 695 (1970).

37. Y. Kato, K. Mima, N. Miyanaga, S. Arinaga, Y. Kitagawa, M. Nakatsuka, and C. Yamanaka, Phys. Rev. Lett. **53**, 1057 (1984).

38. See National Technical Information Service Document No. DOE/SF/19460-117 [Laboratory for Laser Energetics LLE Review **65**, 1 (1995)]. Copies may be obtained from the National Technical Information Service, Springfield, VA 22161.

39. V. N. Goncharov, Phys. Rev. Lett. **82**, 2091 (1999).

40. F. J. Marshall, J. A. Delettrez, R. Epstein, R. Forties, R. L. Keck, J. H. Kelly, P. W. McKenty, S. P. Regan, and L. J. Waxer, Phys. Plasmas **11**, 251 (2004).

41. S. E. Bodner, J. Fusion Energy **1**, 221 (1981).

42. V. N. Goncharov, S. Skupsky, T. R. Boehly, J. P. Knauer, P. McKenty, V. A. Smalyuk, R. P. J. Town, O. V. Gotchev, R. Betti, and D. D. Meyerhofer, Phys. Plasmas **7**, 2062 (2000).

43. R. Epstein, J. Appl. Phys. **82**, 2123 (1997).

44. S. P. Regan, J. A. Marozas, J. H. Kelly, T. R. Boehly, W. R. Donaldson, P. A. Jaanimagi, R. L. Keck, T. J. Kessler, D. D. Meyerhofer, W. Seka, S. Skupsky, and V. A. Smalyuk, J. Opt. Soc. Am. B **17**, 1483 (2000).

45. R. C. Cook, R. L. McEachern, and R. B. Stephens, Fusion Technol. **35**, 224 (1999).

46. R. Betti, V. N. Goncharov, R. L. McCrory, and C. P. Verdon, Phys. Plasmas **5**, 1446 (1998).

47. J. P. Knauer, R. Betti, D. K. Bradley, T. R. Boehly, T. J. B. Collins, V. N. Goncharov, P. W. McKenty, D. D. Meyerhofer, V. A. Smalyuk, C. P. Verdon, S. G. Glendinning, D. H. Kalantar, and R. G. Watt, Phys. Plasmas **7**, 338 (2000).

48. R. Betti, K. Anderson, V. N. Goncharov, R. L. McCrory, D. D. Meyerhofer, S. Skupsky, and R. P. J. Town, Phys. Plasmas **9**, 2277 (2002).

49. D. C. Wilson, C. W. Cranfill, C. Christensen, R. A. Forster, R. R. Peterson, H. M. Hoffman, G. D. Pollak, C. K. Li, F. H. Séguin, J. A. Frenje, R. D. Petrasso, P. W. McKenty, F. J. Marshall, V. Yu. Glebov, C. Stoeckl, G. J. Schmid, N. Izumi, and P. Amendt, Phys. Plasmas **11**, 2723 (2004).

50. G. Dimonte, Phys. Plasmas **6**, 2009 (1999).

51. L. D. Landau and E. M. Lifshitz, *Fluid Mechanics*, 2nd ed., Course of Theoretical Physics, Vol. 6 (Butterworth-Heinemann, Newton, MA, 1987), p. 36.

52. J. G. Wouchuk and R. Carretero, Phys. Plasmas **10**, 4237 (2003).

Figure Captions

FIG. 1. (a) Plastic-shell targets studied in this work. Two thicknesses—20 μm and 27 μm—with D_2 fills are considered. (b) The pulse shape (1-ns square) used to irradiate these targets sets the shell on a relatively high adiabat (~5).

FIG. 2. (a) Acceleration and laser pulse shape history (1-ns square) for the 20-μm CH shell irradiated with a 1-ns square pulse at 23 kJ of energy. (b) Contour plot of the magnitude of the gradient of the natural log of pressure for the target in (a). The darker contours correspond to shock trajectories. The dashed line is the trajectory of the fuel–shell interface. Also shown is the duration of the four phases of the implosion (shock-transit, acceleration, coasting, and deceleration).

FIG. 3. Modal amplitudes of the dominant modes due to beam imbalances as a function of time. The early-time large amplitudes correspond to beam mistiming. The values at the peak of the pulse (0.2–1.1 ns) are due to energy imbalance between beams, beam mispointing, and differences in spot shapes.

FIG. 4. Single-mode amplitudes of the fuel–shell interface at the beginning of acceleration from a 2-D simulation for the 20-μm-thick CH implosion (circles). The values obtained from the model described in Appendix A are also shown (crosses). The "cloudy-day" model relates the amplitudes at the fuel–shell interface to modulation in laser drive. Good agreement between the simulations and model indicate that the seeding of the interface is well understood.

FIG. 5. Nonuniformity spectrum due to phase-plate speckle. This nonuniformity peaks around $\ell \sim 600$.

FIG. 6. Imprint spectrum from single-mode simulations (dotted line) and multimode simulation (solid line). The good agreement confirms linear behavior of imprint. Note that imprint efficiency decreases with increasing mode number. This is opposite in behavior to the laser nonuniformity (Fig. 5).

FIG. 7. Long-wavelength perturbations at the ablation surface due to beam imbalances (solid line) and surface roughness (dotted line) at the start of acceleration. Beam imbalances provide the larger contribution to long-wavelength nonuniformity seeds.

FIG. 8. Amplitudes of the D_2–CH interface versus time for mode numbers 2 and 4 for beam imbalances throughout the pulse (dotted) and beam imbalances imposed on target only until the start of acceleration (solid). The small effect of beam imbalances during the acceleration phase indicates that long-wavelength modes are seeded primarily during shock transit.

FIG. 9. Good agreement is obtained with simulated single-mode growth rates (solid circles) and the Betti formula for plastic (dotted line). Also shown is the Betti formula for growth rates when radiation transport is not included in the simulation (solid line). Reabsorption of radiation from the corona plays an important role in stabilizing the growth of perturbations at the ablation surface.

FIG. 10. Single-mode amplitudes at the end of the acceleration phase. The solid circles are averages of five simulations each with a different choice of random number seed for the nondeterministic SSD model. The error bars represent the standard deviation of the amplitude across the five simulations. The relatively large values of $\ell = 400$ indicate that

such short wavelengths will contribute significantly to the ablation-surface nonuniformity.

FIG. 11. Single-mode growth factors for the coasting phase for the 20-μm-thick (triangles) and 27-μm-thick (squares) CH implosions. The lines are $\sim\sqrt{\ell}$-fit to the growth factors for $\ell < 30$. Growth factors clearly saturate for $\ell > 30$ for the 27-μm-thick CH shell.

FIG. 12. Density profiles at peak neutron production from a 1-D simulation with (dotted) and without (solid) radiation transport. Radiation plays an important role during deceleration by raising the effective Atwood number for long and intermediate wavelengths.

FIG. 13. Modal amplitudes versus time at the fuel–shell interface for the low-order multimode simulation (due to beam imbalances) of a 20-μm-thick CH shell. The interface becomes perturbed shortly after shock breakout around 0.4 ns. A second jump in the amplitude is modeled at ~0.8 ns when the second shock breaks out of the shell. Shorter wavelengths such as modes 6 and 10 decouple during the coasting phase as is indicated by their changing phase. Longer wavelengths (modes 2 and 4) change phase when the shock returns to the interface at ~1.75 ns.

FIG. 14. Density contours at peak neutron production from a multimode simulation including only low-ℓ modes ($\ell < 10$) for the 20-μm-thick CH implosion. An areal-density variation of 23% is calculated at this time in the implosion. The solid line corresponds to the D_2–CH interface.

FIG. 15. Density contours at the end of the acceleration phase for (a) a 20-μm-thick CH shell and (b) a 27-μm-thick CH shell from a multimode simulation of laser imprint. The solid lines correspond to the D_2–CH interface. Note that the shell (indicated by the higher-density contours) is significantly more distorted for the 20-μm implosion than the 27-μm implosion.

FIG. 16. Neutron-production rates from the simulation including only low- and intermediate-mode numbers (dashed–dotted line) and the simulation including short wavelengths (dotted line) compared to 1-D (solid line) for (a) the 20-μm-thick CH shell and (b) the 27-μm-thick CH shell. Note that the addition of mode 200 in the simulation including short wavelengths results in a less-steep fall of the neutron production rate for the 20-μm implosion and retains burn truncation for the 27-μm case.

FIG. 17. Fluid velocity vectors in a frame moving radially in with the fluid overlaid on a contour plot of ion temperature at peak neutron production for the 20-μm-thick CH shell. The simulation, from a single-mode perturbation, illustrates one mechanism for burn truncation. As the velocity vectors indicate, fuel flows into the colder bubbles due to RT growth resulting in burn truncation.

FIG. 18. Density contours for simulations including short wavelengths at peak neutron production for (a) the 20-μm-thick CH shell and (b) the 27-μm-thick CH shell. The solid line is the fuel–shell interface. The short wavelengths ($\ell \sim 200$) have an amplitude of ~1 μm, consistent with estimates of mixing thicknesses from turbulence observations.[50]

FIG. 19. Radial lineouts of density from the simulation including short wavelengths for (a) the 20-μm-thick CH shell and (b) the 27-μm-thick CH shell at two different polar angles [0° (dotted) and 36° (dashed–dotted)], compared to the 1-D simulation (solid line).

Note that the thinner shell has significantly lower densities compared to 1-D. The shell is considerably thicker for the 20-μm implosion. Radial lineouts of temperature are shown for (c) the 20-μm implosion and (d) the 27-μm implosion. All lineouts are at peak neutron production in 1-D. The temperatures in the core are lower than 1-D due to enhanced heat conduction out of the distorted core (both thicknesses) and the overall lower compression in the 20-μm-thick implosion.

FIG. 20. Comparison of calculated (1-D) neutron rates (dotted) with experiment (solid line) for (a) the 20-μm-thick implosion (shot number 30628) and (b) the 27-μm-thick implosion (shot number 22088). Burn truncation is evident for the 27-μm-thick implosion. Neutron production rate persists and is almost as wide as 1-D for the 20-μm-thick implosion.

P. B. Radha
Figure 1

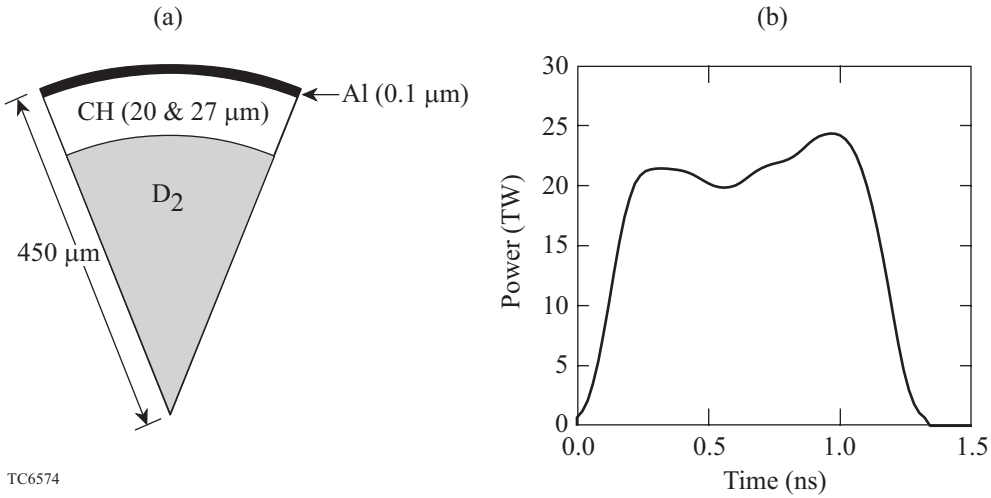

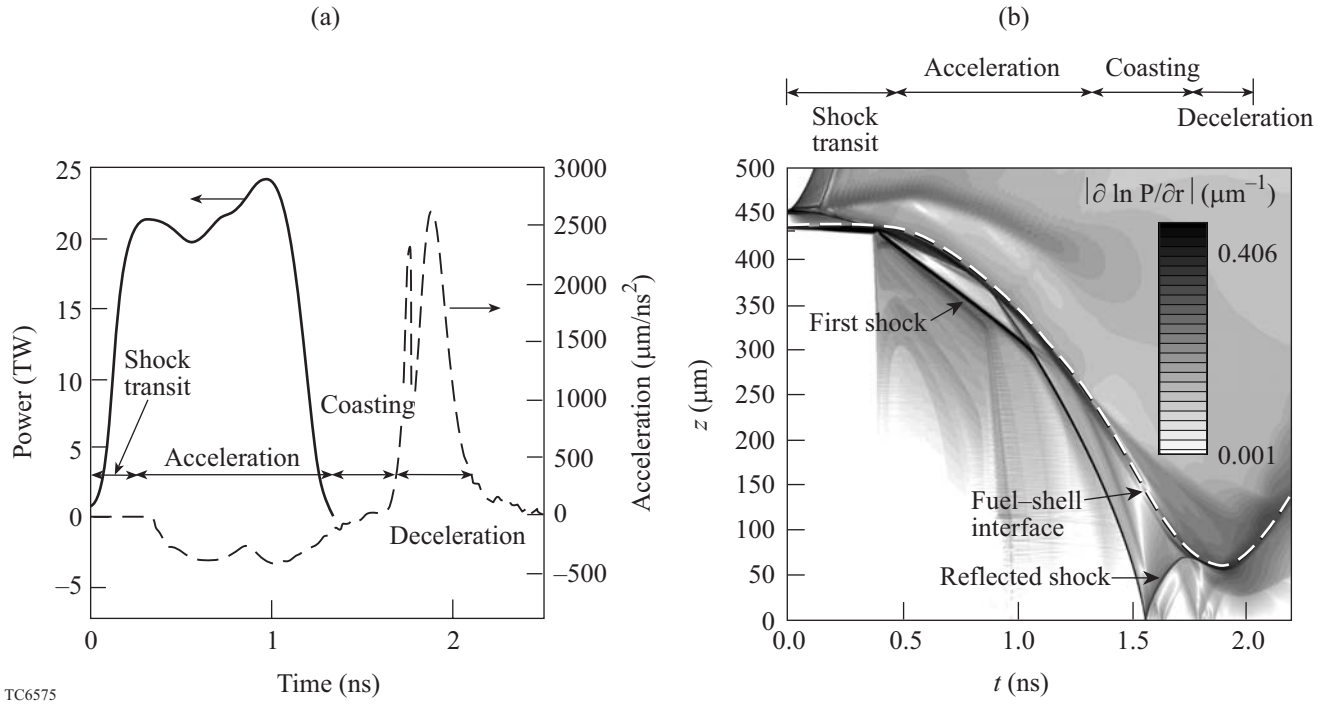
(a)
Power (TW)
Acceleration (μm/ns²)
Time (ns)
Shock transit
Acceleration
Coasting
Deceleration
TC6575
(b)
Acceleration
Coasting
Shock transit
Deceleration
z (μm)
t (ns)
|∂ ln P/∂r| (μm⁻¹)
0.406
0.001
First shock
Fuel–shell interface
Reflected shock

P. B. Radha
Figure 3

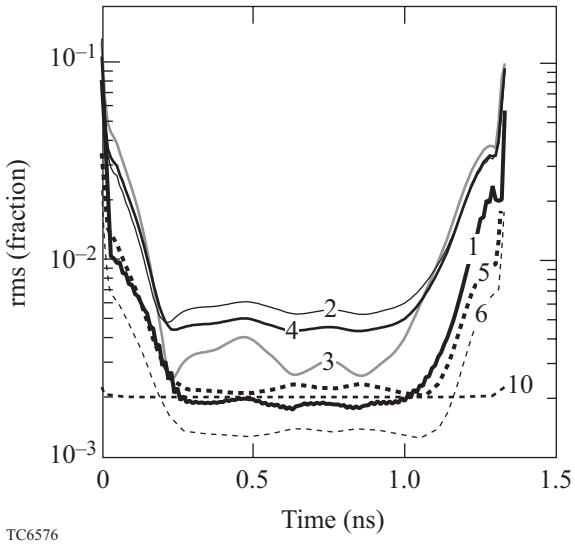

P. B. Radha
Figure 4

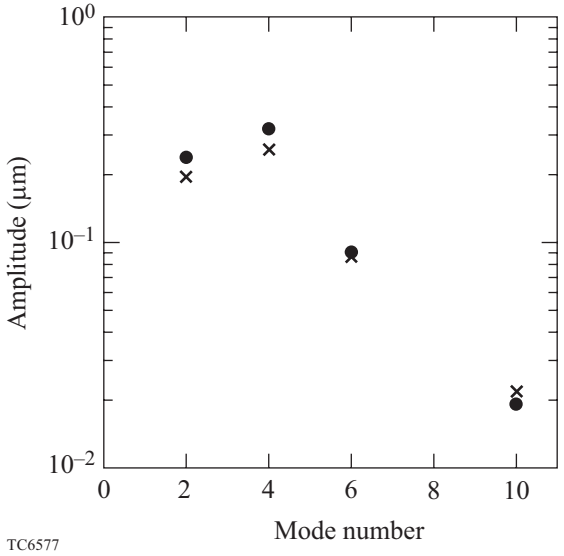

P. B. Radha
Figure 5

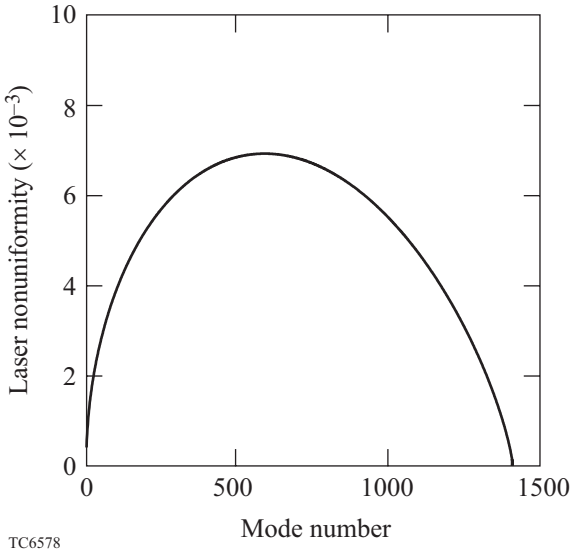

P. B. Radha
Figure 6

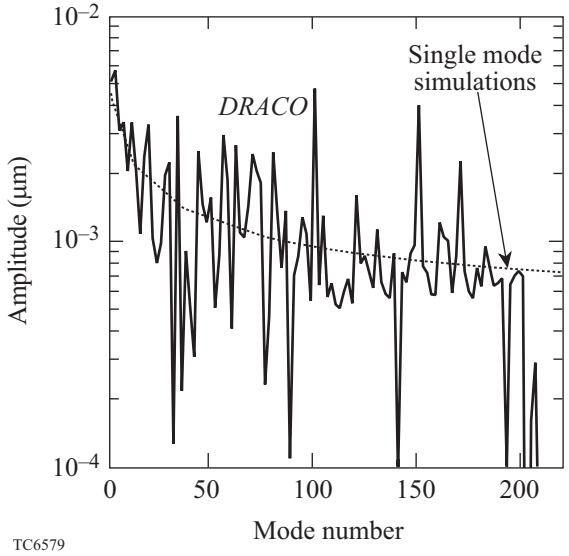

P. B. Radha
Figure 7

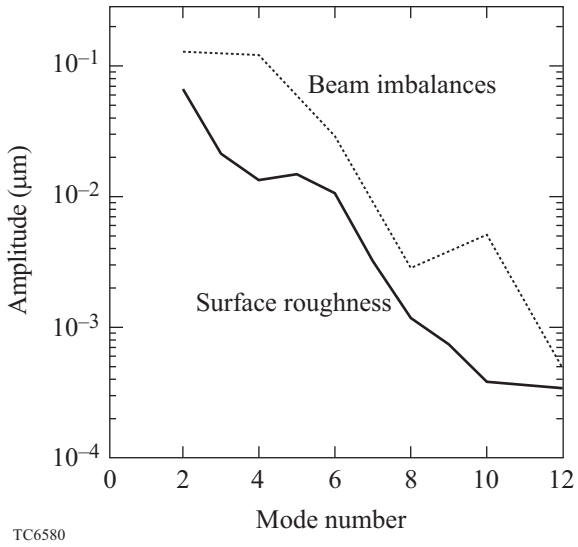

P. B. Radha
Figure 8

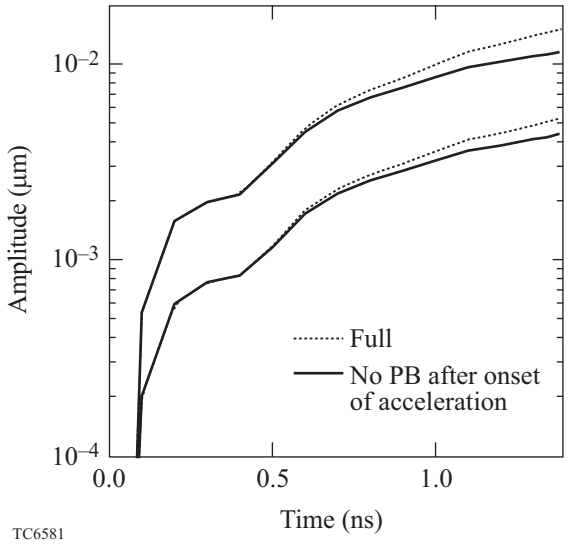

P. B. Radha
Figure 9

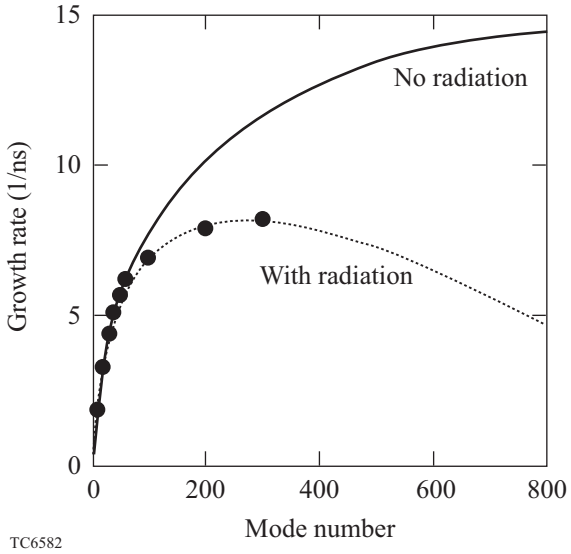

P. B. Radha
Figure 10

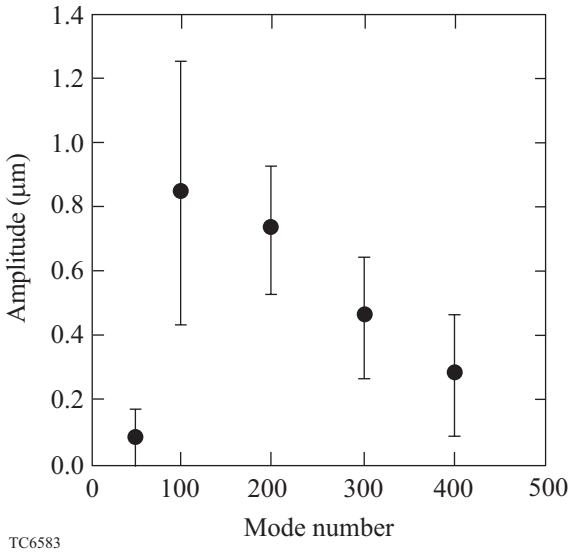

P. B. Radha
Figure 11

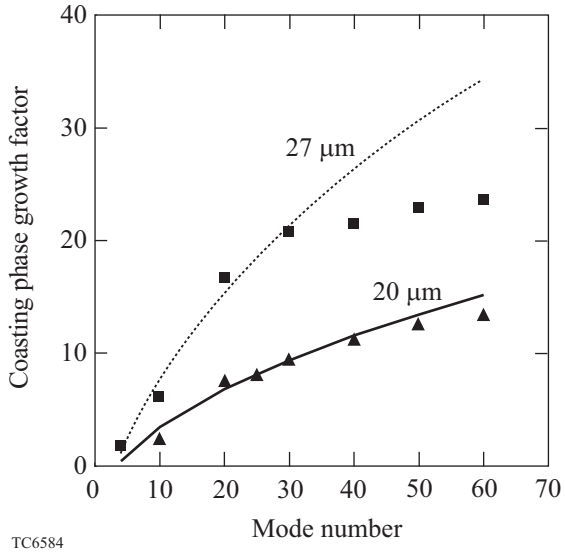

P. B. Radha
Figure 12

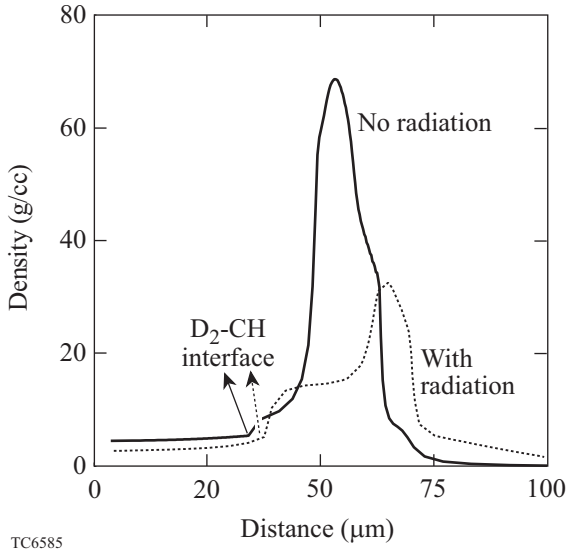

P. B. Radha
Figure 13

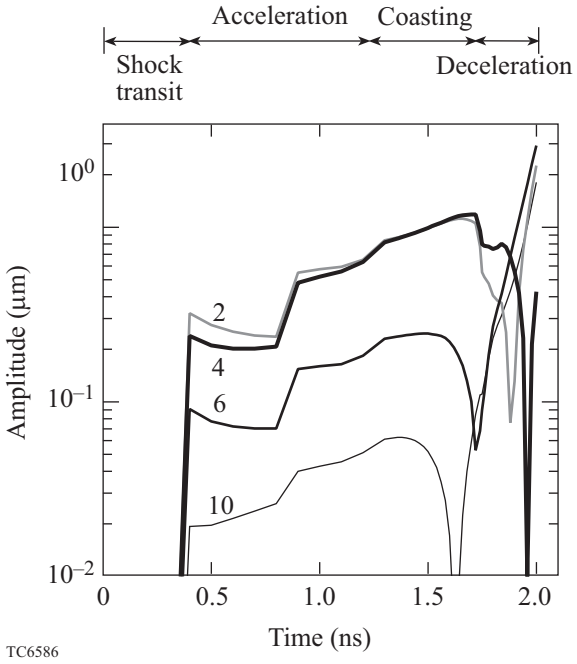

P. B. Radha
Figure 14

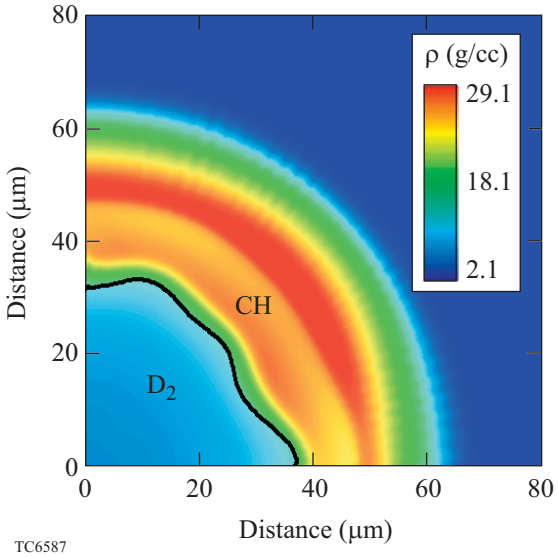

P. B. Radha
Figure 15

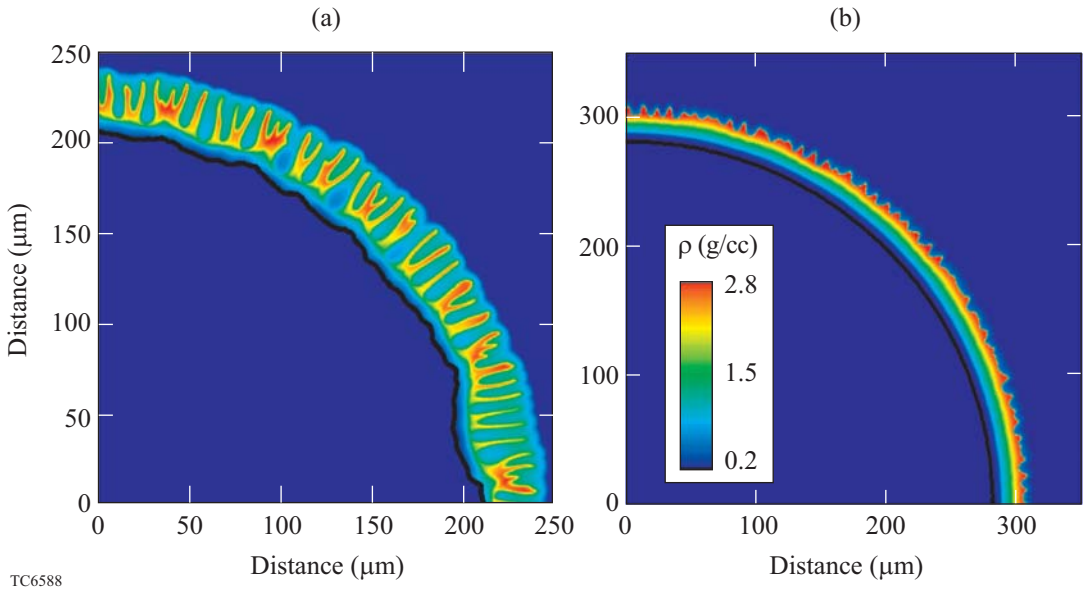

P. B. Radha
Figure 16

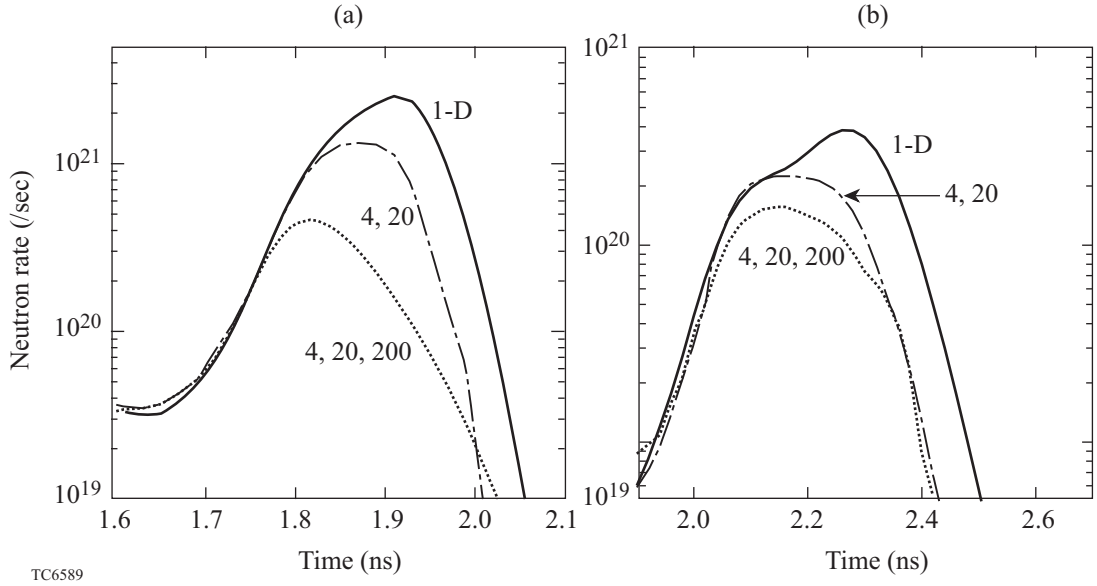

P. B. Radha
Figure 17

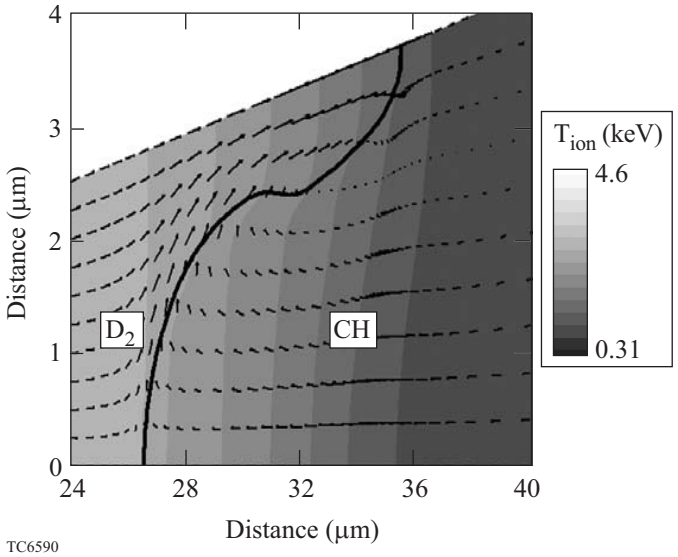

P. B. Radha
Figure 18

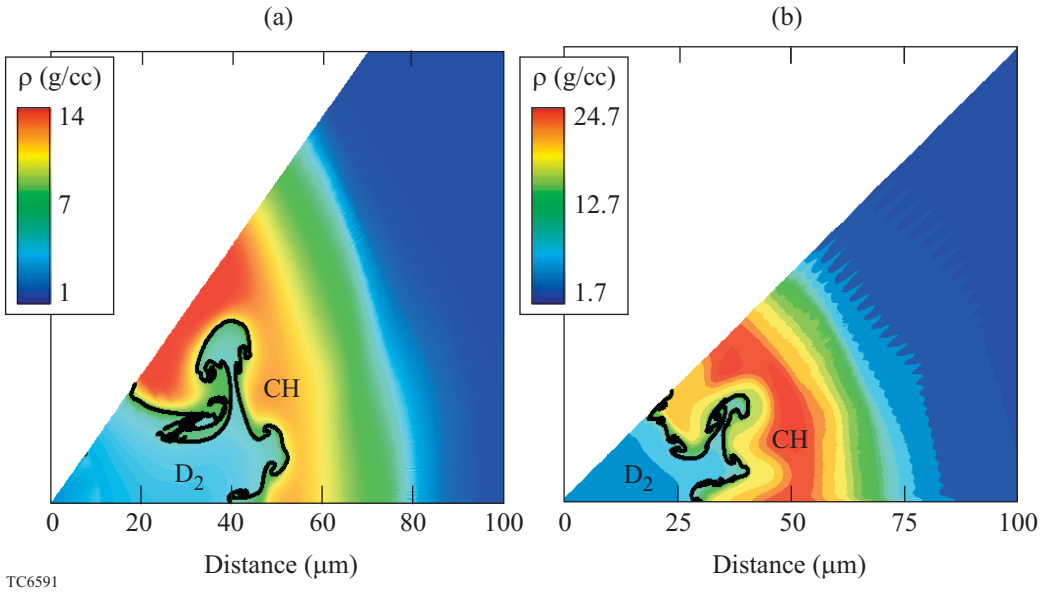

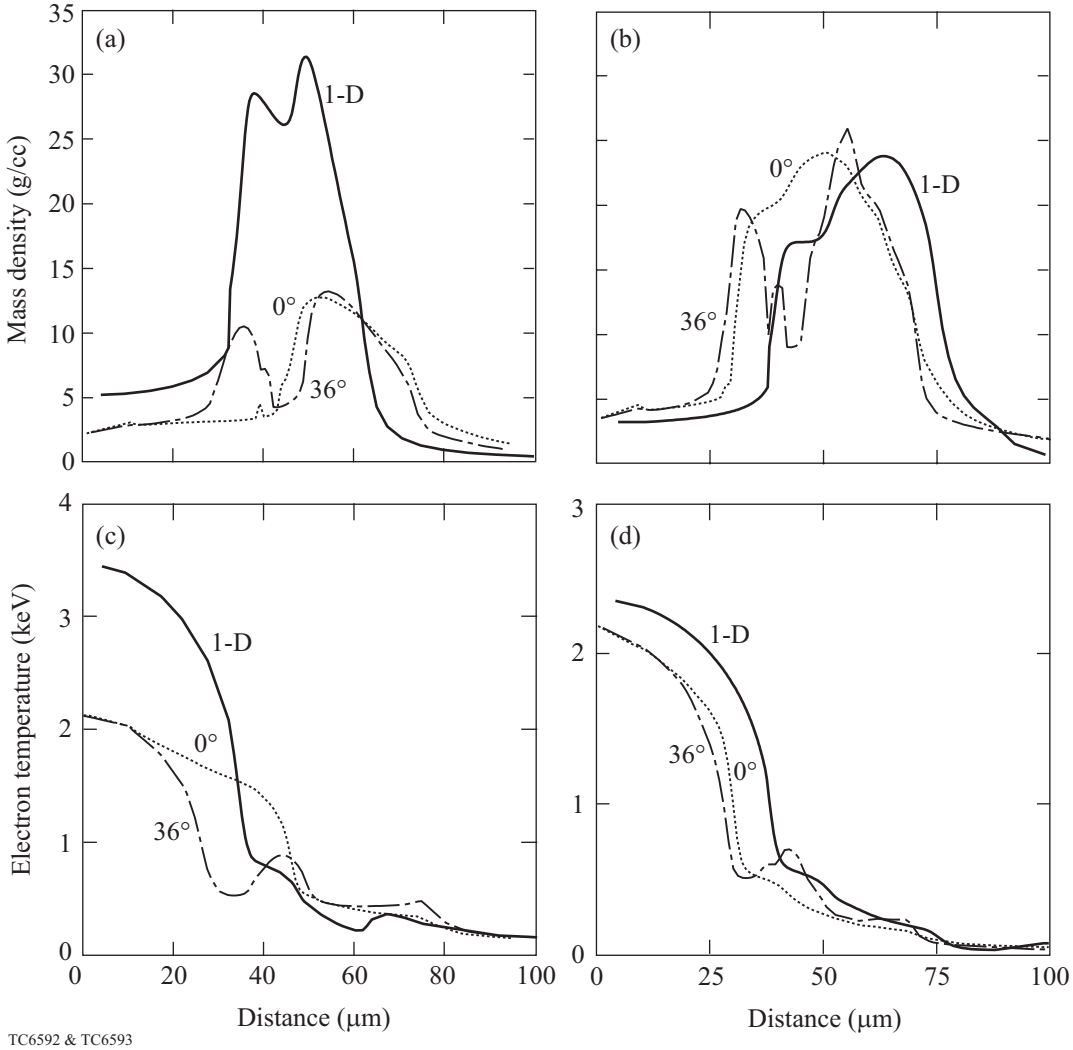
(a)
(b)
(c)
(d)
1-D
0°
36°
Mass density (g/cc)
Electron temperature (keV)
Distance (μm)
Distance (μm)
TC6592 & TC6593

P. B. Radha
Figure 20